Cell Biol Toxicol (2026) 42:71
https://doi.org/10.1007/s10565-026-10188-x

RESEARCH

Single-cell RNA sequencing reveals HMGA2 involvement in neoplastic aggressiveness and endothelial cell senescence in chondrosarcoma

Shenglin Wang · Shuting Lu · Xinwen Wang · Hongxiang Wei · Huarong Zhang · Weixin Zhou · Jie Lin · Xueyi Huang · Fude Liang · Zhaoyang Wu · Jianhua Lin · Xiaopei Shen · Lu Ao

Received: 6 January 2026 / Accepted: 5 April 2026

Abstract Chondrosarcoma (CHS) is a malignant bone tumor resistant to adjuvant treatment, with high-grade patients suffering an unfavorable prognosis. Therefore, a deeper insight into the tumor microenvironment is essential for developing effective treatments for advanced CHS. To decipher the cellular heterogeneity between CHS with differential malignancy and benign cartilage tumors, we performed single-cell RNA sequencing (scRNA-seq) on clinical specimens of high- and low-grade CHS, endochondroma and paratumoral tissues. The findings of transcriptional characteristics were validated by the bioinformatics analyses of public bulk datasets. The role of markers of interest was further explored by histological staining, *in vitro* and *in vivo* experiments. The results demonstrated that neoplastic cells and stromal cells predominated in the CHS tumor microenvironment. High-grade CHS presented aggravated proliferation and angiogenesis characteristics in neoplastic cells. The *in silico* analysis and functional experiments identified HMGA2 as a regulator of these malignant phenotypes and an independent predictor of poor outcome. Tumor-associated endothelial cells (TA-ECs) in CHS demonstrated senescent yet aggressive phenotypes underpinned by HBEGF. Moreover, HCHS exhibited more prevalent

Shenglin Wang, Shuting Lu, Xinwen Wang and Hongxiang Wei contributed equally to this work.

Supplementary Information The online version contains supplementary material available at https://doi.org/10.1007/s10565-026-10188-x.

S. Wang · X. Shen (✉)
The School of Basic Medical Sciences, Fujian Medical University, 1 Xuefu North Road, Fuzhou 350122, China
e-mail: xshen@fjmu.edu.cn

S. Wang
e-mail: shenglinwang0216@163.com

S. Wang · S. Lu · H. Zhang · W. Zhou · J. Lin · X. Shen · L. Ao (✉)
Department of Bioinformatics, Fujian Key Laboratory of Medical Bioinformatics, The School of Medical Technology and Engineering, Fujian Medical University, 1 Xuefu North Road, Fuzhou 350122, China
e-mail: lukey@fjmu.edu.cn

S. Lu
e-mail: l18760360829@163.com

H. Zhang
e-mail: hr_zhang@fjmu.edu.cn

W. Zhou
e-mail: zhouweixin_13@163.com

J. Lin
e-mail: liner0203@163.com

S. Wang · H. Wei · F. Liang · Z. Wu · J. Lin (✉)
Department of Orthopaedics, Fujian Orthopaedics Research Institute, The First Affiliated Hospital of Fujian Medical University, 20 Chazhong Road, Fuzhou 350005, China
e-mail: jianhual123@126.com

H. Wei
e-mail: whxfjmu@163.com

Published online: 11 April 2026

cellular communications between neoplastic cells and TA-ECs mediated by SPP1 and EGF pathways, with SPP1 and HBEGF both predicting unfavorable prognosis. Mechanistically, HMGA2 induced neoplastic secretion of SPP1, which provoked endothelial senescence and HBEGF release. Our findings implicate malignant characteristics in neoplastic cells and endothelial senescence associated with the histological grade of CHS and underscore the potential value of HMGA2 and SPP1 as actionable therapeutic targetes for advanced patients.

Keywords Single-cell RNA sequencing · Chondrosarcoma · High Mobility Group AT-Hook 2 · Senescence · Secreted Phosphoprotein 1

Introduction

Chondrosarcoma (CHS), a highly heterogeneous tumor characterized by the production of cartilage matrix, constitutes the second most common malignancy of bone after osteosarcoma (Chow 2018). CHS can be classified as primary and secondary subtypes, with the latter developing from existing benign cartilaginous tumors such as osteochondroma or enchondroma (Chow 2018). Based on histological subtypes, CHS is further classified as conventional (grades 1–3) and rare (clear cell, mesenchymal, and dedifferentiated) subtypes (Zając et al. 2021). Based on completely surgical resection with wide margins with or without adjuvant therapy, the patient outcome varies according to the clinical, histological and pathological grade. The long-term survival rate is over 53% for patients with low-grade CHS (conventional grades 1–2), 29–55% for those with conventional high-grade CHS (grade 3), but only 7–28% for those with rare high-grade CHS (mesenchymal and dedifferentiated) (MacDonald et al. 2019). Therefore, elucidating the molecular mechanisms underlying CHS aggressiveness is essential for improving patient outcomes.

The crosstalk between tumor cells and their microenvironment constitutes a critical driver of tumor progression. In most tumors, $CD8^+$T cells and proinflammatory M1 macrophages exert antitumor effects, whereas Treg cells and M2 macrophages may promote tumor progression (Gordon and Martinez 2010). Modulation of the immune microenvironment is also involved in CHS invasiveness. Low-grade non-invasive CHS was found to be surrounded by a high level of $CD8^+$T cells, whereas high-grade invasive cases were predominantly infiltrated by $CD163^+$(M2) macrophages (Simard et al. 2017). According to the CHS classification by immune-microenvironment phenotypes, tumor subtypes with exhausted T cells and dendritic cells showed better response to PD-1 immune therapy (Li et al. 2021). Fibroblasts and endothelial cells, among other components of the tumor microenvironment, also contribute significantly to tumor malignancy (Tiwari et al. 2022). However, the heterogeneity of mesenchymal composition and immune functions for CHS remain poorly understood.

Single-cell RNA sequencing (scRNA-seq) enables the dissection of transcriptional heterogeneity across cell types by capturing cellular gene expression profiles (Baslan and Hicks 2017). scRNA-seq has been applied to explore the microenvironment of tumors, such as breast cancer (Sun et al. 2023), pancreatic ductal adenocarcinoma (Wang et al. 2023), and lung cancer (Hu et al. 2023). Due to the low prevalence of CHS, there is a scant study on this disease by scRNA-seq. Recently, Su et al. mapped conventional

F. Liang
e-mail: 1150212963@qq.com

Z. Wu
e-mail: zywu93@126.com

S. Wang · X. Shen · L. Ao
Key Laboratory of Gastrointestinal Cancer (Fujian Medical University), Ministry of Education, Fuzhou 350122, China

X. Wang
Department of Orthopaedics, Sanming First Hospital Affiliated to Fujian Medical University, Sanming 365001, China
e-mail: andrewbread@163.com

H. Wei
Department of Orthopaedics, National Regional Medical Center, Binhai Campus of the First Affiliated Hospital of Fujian Medical University, Fuzhou 350212, China

X. Huang
The School of Health, Fujian Medical University, Fuzhou 350122, China
e-mail: 1730170732@qq.com

X. Shen · L. Ao
Institute of Precision Medicine, Fujian Medical University, Fuzhou 350122, China

central CHS at single-cell resolution, demonstrating that endoplasmic reticulum stress critically promotes malignant transformation (Su et al. 2024). However, the study focused on chondrocytes, leaving the features of the tumor microenvironment in disease progression unclarified.

Here, we characterized the single-cell transcriptomic landscapes of high-grade CHS, low-grade CHS, peritumoral tissues, and enchondroma. In high-grade CHS, neoplastic cells exhibited aggravated malignant characteristics while decreased chondrogenesis. HMGA2 in neoplastic cells was found to be an independent predictor for unfavorable outcome of patients and was validated to facilitate the malignant behaviors. TA-ECs in CHS demonstrated senescent yet aggressive phenotypes with the involvement of HBEGF. Additionally, high-grade CHS presented more intensive cellular communications between neoplastic cells and TA-ECs mediated by SPP1 and EGF pathways, with SPP1 and HBEGF both associated with adverse outcome. HMGA2 may release SPP1, inducing senescence in endothelial cells and HBEGF secretion. Our study reveals malignant features in neoplastic cells and senescent conversion of tumor-associated endothelium in the CHS microenvironment, providing a clue for understanding tumor invasion and positioning HMGA2- and SPP1-targeted therapy for patients with advanced disease.

Materials and methods

Human specimens

A total of ten patients were included for single-cell sequencing in this study, of which eight were pathologically diagnosed with CHS and two with enchondroma (ECH). The histopathology of all cases was confirmed via hematoxylin–eosin staining. Tumor tissues were obtained by surgical resection from two benign ECH, three low-grade CHS (LCHS) and three high-grade CHS (HCHS). Peritumoral tissues (NCHS) were obtained from two additional LCHS. Patients had not received antitumor therapy before surgery. The study adhered to the Declaration of Helsinki, and the Ethics Committee of the First Affiliated Hospital of Fujian Medical University approved the protocols involving human samples. Written informed consent was obtained from all participants. Clinical details are presented in Table S1.

Single-cell sequencing

The single-cell solution was prepared and sequenced by the 10X Genomics Chromium Single-Cell 3′ Kit (V3) following a previously established protocol (Wang et al. 2024). The CellRanger software (version 6.0.0, 10X Genomics) was used to generate gene-barcode matrices. Cells were filtered out if they exhibited any of the following: < 200 detected genes, gene or UMI counts in the top 2%, or > 10% mitochondrial gene expression. Genes expressed in fewer than five cells were also filtered out. After log-normalization and scaling, principal component analysis (PCA) was performed on the filtered count matrix. Following dimensionality reduction, unsupervised clustering was performed, with results visualized by Uniform Manifold Approximation and Projection (UMAP). Batch effects across samples were corrected with Harmony (version 1.0) (Korsunsky et al. 2019) prior to sample integration, with the exception of neoplastic cells to retain genuine intertumoral heterogeneity. DoubletFinder was used to identify and remove potential multiplets from the dataset (McGinnis et al. 2019). Samples of fewer than 30 cells were not included in subsequent analyses.

RNA sequencing (RNA-seq)

Total RNA extraction was performed with TRIzol reagent (Sangon Biotech, Shanghai, China), with the cDNA library constructed using the NEBNext Ultra II RNA Library Prep Kit for Illumina (New England Biolabs Inc., MA, USA). Transcriptome sequencing was conducted on the Illumina NovaSeq Xplus platform at Bioprofile Gene Technology (Shanghai, China).

Differentially expressed genes (DEGs)

Single-cell DEGs (min.pc > 0.10, logFC > 0.25, FDR-adjusted P-value < 0.05, and only.pos = T) were analyzed using the FindAllMarkers() and FindMarkers() functions in the Seurat package (version 3.1.2) (Butler et al. 2018). For RNA-seq analysis, DEGs were defined by DESeq2 using criteria of $P < 0.05$ and |log2FC| > 0.58 or 1.

Mfuzz clustering analysis

Soft clustering analysis of gene expression patterns across multiple groups was performed using the Mfuzz algorithm. Optimal clusters were identified by minimum centroid distance and subsequently used for functional enrichment analysis and signature scoring.

Pseudotime analysis

The Monocle2 package (version 2.99.3) (Qiu et al. 2017) was utilized with default settings to infer the cell developmental trajectory.

Scoring of signature

Based on literature-reported marker genes associated with specific features, we estimated the potential biological functions of the cells of interest. For single-cell data, the UCell software package (version 2.6.0) (Andreatta and Carmona 2021) was used to estimate the single-cell signature score or the average score for all cells per sample. For bulk sequencing data, the ssGSEA algorithm was applied to estimate the signature score for each sample.

Copy number variation analysis

We estimated chromosomal copy number variations (CNVs) in individual chondrocytes using the InferCNV package (version 1.8.1) (Patel et al. 2014) to distinguish neoplastic from non-neoplastic cells. The chondrocytes were used for the observations, with lymphocytes (T/NK cells) used as the reference. Genes expressed in > 20 cells were sorted by chromosomal location. Expression values were normalized (centered at 1, thresholded at 1.5 standard deviations) and smoothed using a 101-gene sliding window.

Identification of transcription factors

The gene regulatory networks and activated transcription factors for neoplastic cells were inferred using the SCENIC package (version 1.1.3) (Aibar et al. 2017) based on the gene-barcode matrices. The co-expression network was calculated using GRNBoost2 and the regulons were then identified using RcisTarget. AUCell was used to score the activity of the regulons for each cell.

Pathway enrichment analysis

Using the clusterProfiler package (version 4.6.2) (Yu et al. 2012), we performed enrichment analysis and considered pathways with $P < 0.05$ significant.

Cell–cell interaction analysis

The intercellular communications between different cell subtypes were estimated by the CellChat (version 1.5.0) (Jin et al. 2021) package following a previously described protocol (Wang et al. 2024).

Analyses based on public bulk mRNA profiles

Bulk mRNA profiles were retrieved from The Cancer Genome Atlas (TCGA-SARC), EBML-EBI (E-MTAB-7264), the Gene Expression Omnibus (GSE12475, GSE202361) and the Cancer Cell Line Encyclopedia (CCLE) databases. Kaplan–Meier survival analysis and optimal expression cutoff determination for patient stratification were conducted with the "survival" (version 3.5–5) and "survminer" (version 0.4.9) packages, respectively, with the latter selecting the threshold that maximizes the log-rank test statistic.

Cell culture

The CHS cells SW1353 (low grade), HT1080 (high grade) and endothelial cells HUVEC were obtained from the Stem Cell Bank, Chinese Academy of Sciences (Shanghai, China). Cells were maintained in DMEM with 10% fetal bovine serum (FBS, VivaCell, Shanghai, China) and 1% penicillin–streptomycin in a humidified atmosphere of 5% CO_2 at 37 °C.

Immunohistochemical staining

Archival FFPE specimens of primary tumor tissues were collected to perform immunohistochemistry by applying an Elivision™ plus Polyer HP Kit (Maixin Biotechnologies, Fuzhou, China). The Sects. (4-μm thick) underwent deparaffinization, rehydration and blockage of endogenous peroxidase activity. Following heat-induced antigen retrieval, the sections were incubated overnight at 4 ℃ with antibodies against CD45 (60287–1-Ig; 1:5000; Proteintech, Wuhan, China), HMGA2 (ab207301; 1:200; Abcam, Cambridge, UK),

and HBEGF (ab218019; 1:200; Abcam). After treatment with a polymer helper reagent for 20 min, sections were incubated with poly-peroxidase-anti-mouse/rabbit IgG for 30 min at room temperature. Finally, staining was performed with diaminobenzidine (Maixin Biotechnologies), followed by dehydration and mounting. Staining was scored by multiplying the intensity grade (0–3: none, weak, moderate, strong) by the percentage grade (0–4: $<5\%$, 5–24%, 25–50%, 51–74%, $\geq 75\%$).

Multiplex immunofluorescence

Staining was performed using the Opal Multiplex IHC kit (Akoya Biosciences, NEL861001KT). Tissue slides underwent deparaffinization, rehydration and microwave antigen retrieval, followed by incubation with primary antibodies against CD31 (66,065–2-Ig; 1:200; Proteintech), and P21 (82,669–2-RR; 1:100; Proteintech). After incubation with secondary antibodies and Opal fluorophores, nuclei were stained with DAPI, and slides were imaged using the Vectra Polaris multispectral Imaging System (Akoya Biosciences).

Lentivirus transfection

Lentiviral particles (Genechem, Shanghai, China) for HMGA2 overexpression (oe-HMGA2), knockdown (sh-HMGA2), or control were used to infect CHS cells as per the manufacturer's protocol. Efficiency was evaluated by RT-qPCR and Western blot.

Quantitative real-time PCR (RT-qPCR)

Total RNA was extracted using TRIzol (Sangon Biotech, Shanghai, China), and reversed into cDNA with Maxima Reverse Transcriptase (Thermo Scientific, USA). qPCR was performed using the $2\times$SG Fast qPCR Master Mix (High Rox) (Sangon Biotech) and analyzed on an ABI 7500 thermocycler (Waltham, MA, USA). Relative Ct values were normalized to β-actin. Relevant primer sequences are provided in Table S2.

Cell proliferation assay

Cell viability was measured by the CCK8 (New Cell & Molecular Biotech, Suzhou, China) assay per the manufacturer's protocol.

Colony formation assay

CHS cells seeded in six-well plates were incubated for 6 days. After gentle rinsing with PBS, cells were fixed in 70% ethanol and stained with 0.1% crystal violet (Solarbio, Wuhan, China). Colonies exceeding 50 cells were counted microscopically.

Wound healing assay

CHS cells seeded in six-well plates were wounded by scraping the monolayer with a 200-μL pipette tip. After 24 h, cells were fixed, stained with 0.1% crystal violet (Solarbio), and migrating cells were counted microscopically.

Cell apoptosis assay

Apoptosis was assessed by flow cytometry using the Annexin V-FITC Apoptosis Detection Kit (Beyotime) on an Accuri C6 flow cytometer (BD Biosciences, Franklin Lakes, NJ, USA).

Western blot

Protein isolation and quantification were performed using the Membrane and Cytosol Protein Extraction Kit and the Bicinchoninic Acid (BCA) Protein Assay Kit (both from Beyotime). After separation on 10% SDS-PAGE gels, proteins were transferred to PVDF membranes (Millipore, MA, USA), blocked for 15 min with NcmBlot blocking buffer (New Cell & Molecular Biotech), and incubated overnight at 4 °C with primary antibodies against HMGA2 (ab207301, 1:200; Abcam) and Tubulin (66,031–1-Ig, 1:10,000; Proteintech). After incubation with HRP-conjugated secondary antibodies (Proteintech) for 1 h at room temperature, signals were detected with Enhanced Chemiluminescent reagent (New Cell & Molecular Biotech) on a FluorChem R system (ProteinSimple, USA).

Oxidative stress and redox balance assessment

Intracellular ROS were visualized with the ROS Assay Kit (Beyotime) under a fluorescence microscope. Lipid peroxidation was quantified by

malondialdehyde content using the MDA kit (Beyotime), and glutathione status was assessed with the GSH/GSSG Assay Kit (Beyotime).

Senescence-associated β-galactosidase staining

HUVEC cells seeded into 6-well plates were cultured for 72 h in conditioned medium from SW1353 or HT1080 cells. SA-β-Gal activity was detected using the Senescence β-Galactosidase Staining Kit (Beyotime).

Xenograft tumor growth assay

Female BALB/C nude mice (4 weeks old; Shanghai SLAC Laboratory Animal Co., Ltd., Shanghai, China) were housed in specific pathogen-free conditions with free access to food and water. Animal experiments were authorized by the Animal Research Committee of the Fujian Medical University and performed in line with the official guidelines. SW1353 cells or HT1080 cells (100 μL, 1×10^6 cells) were combined with 300 μL Matrigel™ (BD Biosciences) and injected subcutaneously into the backs of mice. At 5 weeks, tumors were excised and volume calculated as $(\text{length}\times\text{width}^2)/2$.

Statistical analysis

Statistical analyses were performed using R software (version 4.2.3) or GraphPad Prism 8.0.1 (San Diego CA, USA). Differences between two groups were evaluated by unpaired Student's t-test or Wilcoxon rank-sum test (with Benjamini–Hochberg adjustment for multiple testing), while one-way ANOVA with Tukey's HSD post-hoc test was used for multiple pairwise comparisons among groups. Spearman's correlation test was employed for correlation analyses. Statistical significance was defined as a two-sided $P<0.05$.

Results

Cellular heterogeneity of enchondroma and CHS at single-cell resolution

To characterize the distinct microenvironmental landscapes of CHS across different malignancy grades, we performed single-cell RNA sequencing (scRNA-seq). An overview of the study workflow is outlined in Fig. 1A. A total of 81,943 cells remained, with a median of 2,950 genes and 8,818 UMIs per cell (Fig. 1B, Fig. S1A). Based on canonical marker gene expression, cells were separated into 11 cell types: chondrocytes, endothelial cells (ECs), fibroblasts, mural cells, myocytes, mononuclear phagocytes (MPs), neutrophils, mast cells, B cells, plasma cells, and T/NK cells (Fig. 1B and C, Fig. S1B). Cellular diversity was observed regarding the distribution of cell types across groups. Stromal cells including endothelial cells, fibroblasts, and myocytes, consisted the majority of the NCHS samples. LCHS exhibited the highest chondrocytes infiltration alongside the lowest proportion of immune cells (Fig. 1D-F, Fig. S1C-F), a pattern that may reflect the sparse immune cell infiltration characteristic of cartilaginous nodules (Simard et al. 2017). Notably, HCHS showed an accumulation of MPs compared to LCHS (Fig. 1D and E, Fig. S1C-F), which might contribute to tumor invasiveness, as previously suggested (Simard et al. 2017). It should be noted, however, that the findings regarding HCHS are based on a relatively limited sample size with constrained histological heterogeneity. Further validation in expanded cohorts would be valuable to confirm these preliminary observations.

Malignant features of neoplastic cells associated with CHS aggressiveness

In this study, 34,645 chondrocytes were annotated into seven clusters (Fig. 2A), with their top differentially expressed genes shown in Fig. S2A. All seven clusters exhibited elevated CNV scores, indicating their neoplastic nature (Fig. S2B and C). Based on canonical marker expression, clusters Chon1-Chon4 were identified as well-differentiated neoplastic chondrocytes. These clusters were characterized by the expression of cartilage development-associated genes (COL2A1, ACAN, and COMP) (Fig. 2B, Fig. S2E) and neoplastic markers (Fig. S2D)(Kim et al. 2020; Nakagawa et al. 2025; Su et al. 2024; Yin et al. 2024). The High1 and High2 clusters were characterized as progenitors expressing proliferative genes (CDH2, CCND1, and CCND2) (Fig. 2B, Fig. S2E) (Tanaka et al. 2023). The High3 cluster represented fibrocartilage neoplastic cells,

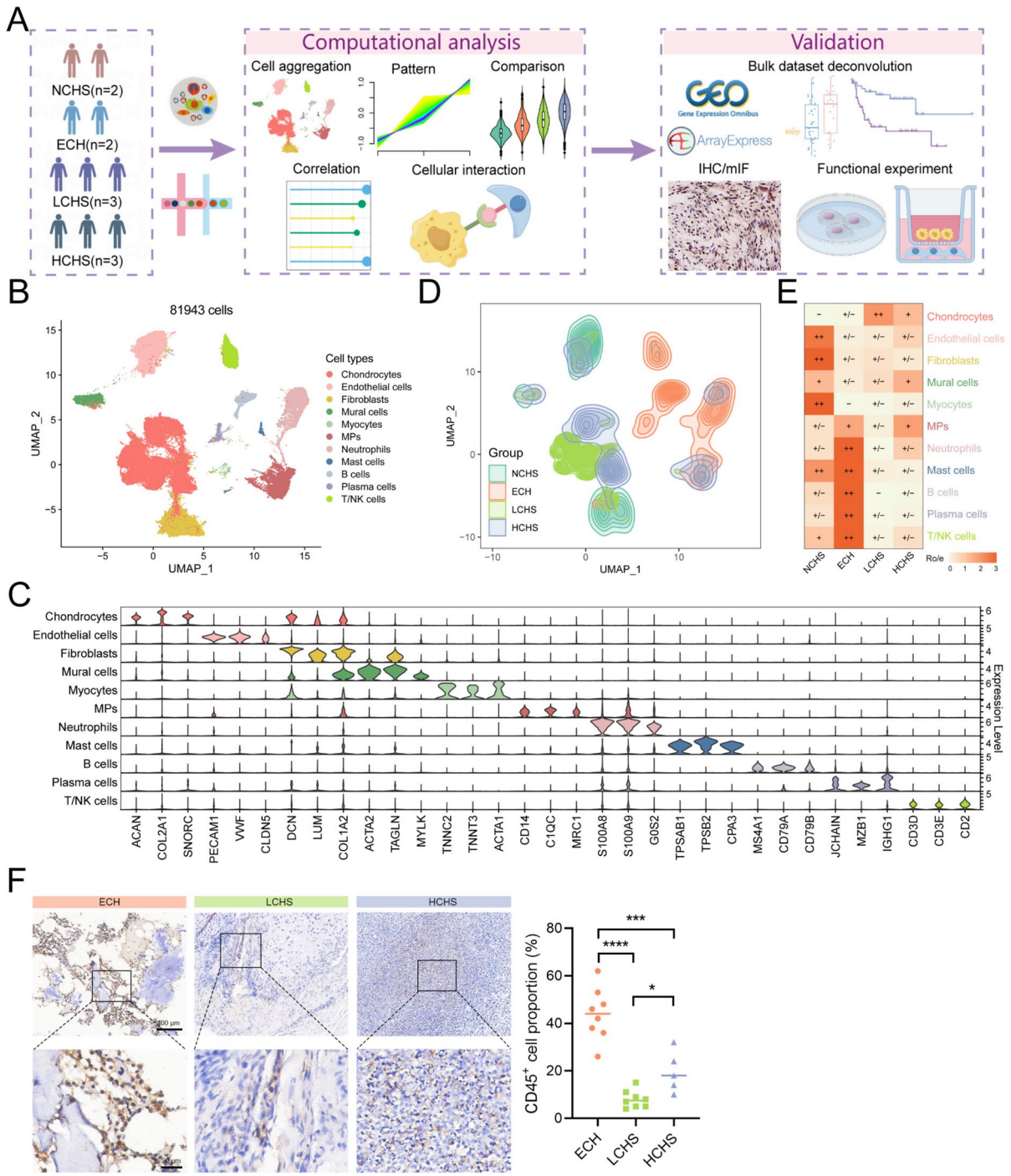

Fig. 1 Single-cell transcriptomic atlas of cartilage tumors. **A** Schematic overview of the study workflow. Part of the image was adapted from the Figdraw platform. **B** Uniform Manifold Approximation and Projection (UMAP) plot showing 81,943 cells from all samples annotated as 11 cell types. **C** Violin plot displaying the expression levels of canonical marker genes across cell types. **D** Density plot corresponding to (B) highlighting cell type distribution across groups. **E** Ro/e analysis showing the inferred relative enrichment of cell types. **F** Representative immunohistochemistry images (left) and corresponding quantification (right) validating $CD45^+$ cell infiltration across groups from our cohort. Scale bar: 100 μm (200×) and 20 μm (400×). $^*P<0.05$; $^{***}P<0.001$; $^{****}P<0.0001$ by one-way ANOVA with post-hoc test

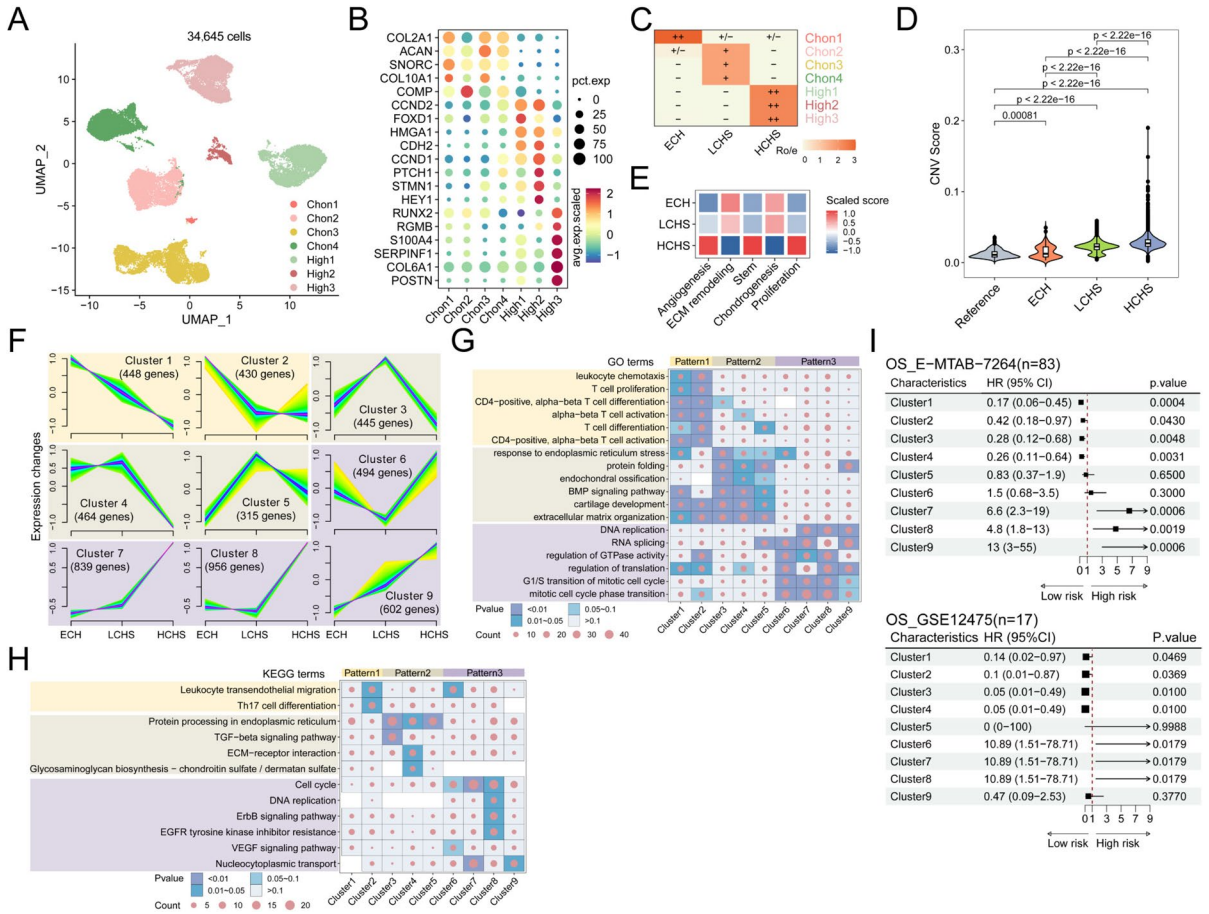

Fig. 2 Malignant characterization of neoplastic cells for CHS aggression. **A** UMAP plot showing 34,645 cells annotated as 7 subtypes. **B** Dot plot displaying the scaled average expression of selected genes across cell subtypes. **C** Ro/e analysis showing the inferred relative abundance of cell subtypes. **D** Violin-box plot showing the inferred copy number variation (CNV) score across groups. Boxes represent the interquartile range, with horizontal lines indicating the median and whiskers representing the min–max range. Statistical significance was determined by Wilcoxon tests with Benjamini–Hochberg correction. **E** Heatmap illustrating the scaled score of interested signatures across groups. **F** Mfuzz clustering analysis identifying genes with dynamic expression patterns in neoplastic cells across groups. **G-H** Gene Ontology (GO) (G) and Kyoto Encyclopedia of Genes and Genomes (KEGG) (H) enrichment analysis of the genes associated with each Mfuzz cluster from (F). **I** Forest plot showing the association of the Mfuzz cluster-specific gene signatures with patient overall survival in independent CHS cohorts

displaying increased expression of fibroblast-associated genes (S100A4, COL6A1, and POSTN) alongside decreased expression of cartilaginous matrix genes (Fig. 2B, Fig. S2E). Consistent with a recent study (Su et al. 2024), well-differentiated neoplastic chondrocytes were enriched in both ECH (Chon1) and LCHS (Chon2-Chon4). In contrast, HCHS was primarily composed of the High1, High2 and High3 clusters (Fig. 2C, Fig. S3A and B). These grade-specific distribution patterns highlight the transcriptional heterogeneity underlying CHS malignancy.

Notably, HCHS exhibited higher CNV scores than LCHS and ECH (Fig. 2D). Functionally, HCHS presented the lowest signature scores regarding ECM remodeling and chondrogenesis, yet the highest scores regarding angiogenesis, stemness, and proliferation (Fig. 2E). To delineate the transcriptional programs related to CHS aggressiveness, we performed Mfuzz clustering analysis (Fig. 2F). Genes highly expressed in LCHS (clusters 3–5) were enriched in pathways related to endochondral ossification, cartilage development,

and extracellular matrix organization. While those upregulated in HCHS (clusters 6–9) were associated with cell cycle transition, DNA replication, ErbB pathway, and VEGF pathway (Fig. 2G and H). Additionally, gene signatures from clusters 1–4 were associated with good prognosis, while those from clusters 7 and 8 were associated with an unfavorable outcome (Fig. 2I). These findings suggest that CHS progression is characterized by the suppression of chondrocyte differentiation, accompanied by enhanced pro-angiogenetic, proliferative, and mesenchymal features.

HMGA2 is associated with malignant characteristics in CHS cells

To identify vital genes associated with CHS progression, we first screened for activated transcription factors (TFs) in neoplastic cells and their targeted genes. The target genes were then intersected with genes from clusters 7–8 identified by Mfuzz analysis, as well as with neoplastic-cell-specific genes (Fig. 3A). This intersection yielded 152 genes, regulated by 104 TFs (Fig. 3A). Notably, HMGA2, specifically expressed in neoplastic cells, displayed a stepwise increase in both expression level and transcriptional activity from ECH to HCHS (Fig. 3B and C, Fig. S3C). Preferential HMGA2 upregulation in high-grade CHS was validated in public datasets (Fig. 3D) and further confirmed in our cohort by immunohistochemistry (Fig. 3E). Correlation analysis demonstrated a positive association between HMGA2 expression and malignancy-related features, including cell proliferation, stemness, and angiogenesis (Fig. 3F and G). Moreover, High HMGA2 expression independently predicted worse progression-free and overall survival in CHS patients (Fig. 3H, Fig. S3D and E). In low-grade (G1 + G2) CHS patients, elevated HMGA2 expression also correlated with malignant characteristics and predicted unfavorable prognosis (Fig. 3I and J, Fig. S3F). Given that HMGA2 has been implicated in regulating cell cycle, DNA damage repair, epithelial-mesenchymal transition, and chemotherapy resistance (Zhang et al. 2019), these findings indicate HMGA2 as a potential contributor to CHS malignancy.

HMGA2 overexpression promotes proliferation and ferroptosis resistance in low-grade CHS

According to the CCLE dataset, CHS cell lines presented elevated HMGA2 expression compared to normal chondrocytes, especially for HT1080 cells, which was validated by RT-qPCR and Western blotting (Fig. 4A and B, Fig. S4A). To determine the role of HMGA2 in low-grade CHS progression, we overexpressed it in SW1353 cells (Fig. 4C, Fig. S4B) and assessed the resulting phenotypic changes. HMGA2 overexpression markedly enhanced cell proliferation, colony formation, and migratory capacity (Fig. 4D-F). In vivo, HMGA2 overexpression promoted tumor growth and increased tumor weight in a subcutaneous xenograft model (Fig. 4G and H). To elucidate the underlying mechanisms, we performed transcriptomic sequencing comparing oe-HMGA2 and oe-NC groups (Fig. S4C and D). Upregulated genes in the oe-HMGA2 group were predominantly associated with mitochondrial metabolism, reactive oxygen species, and peroxisome activity, while those upregulated in the oe-NC group were mainly related to cell adhesion and immune cell differentiation (Fig. S4E). Notably, HMGA2-overexpressing cells presented reduced expression of genes involved in oxidative stress, iron metabolism, fatty acid metabolism, and lipid metabolism, alongside enhanced expression of glutathione metabolism genes (Fig. 4I). Furthermore, HMGA2 overexpression upregulated ferroptosis suppressor genes while downregulating genes that promote ferroptosis induction (Fig. 4I). To functionally validate ferroptotic engagement, we challenged SW1353 cells with the canonical ferroptosis inducer RSL3. Cells overexpressing HMGA2 tolerated RSL3-triggered proliferation arrest and cell death (Fig. 4J and K). In line with these observations, HMGA2-overexpressing cells displayed a ferroptosis-resistant metabolic profile upon RSL3 treatment, characterized by a higher GSH/GSSG ratio and reduced accumulation of MDA and ROS (Fig. 4L-N). Functionally, the cytoprotection and reduced MDA accumulation conferred by HMGA2 were both attenuated by the ferroptosis inhibitor Ferrostatin-1 (Fer-1), supporting the specificity of this phenotype (Fig. S4F and G). At the molecular level, HMGA2 overexpression upregulated ferroptosis suppressors (HMOX1, GPX4) while repressing the ferroptosis driver ACSL4 (Fig. 4O).

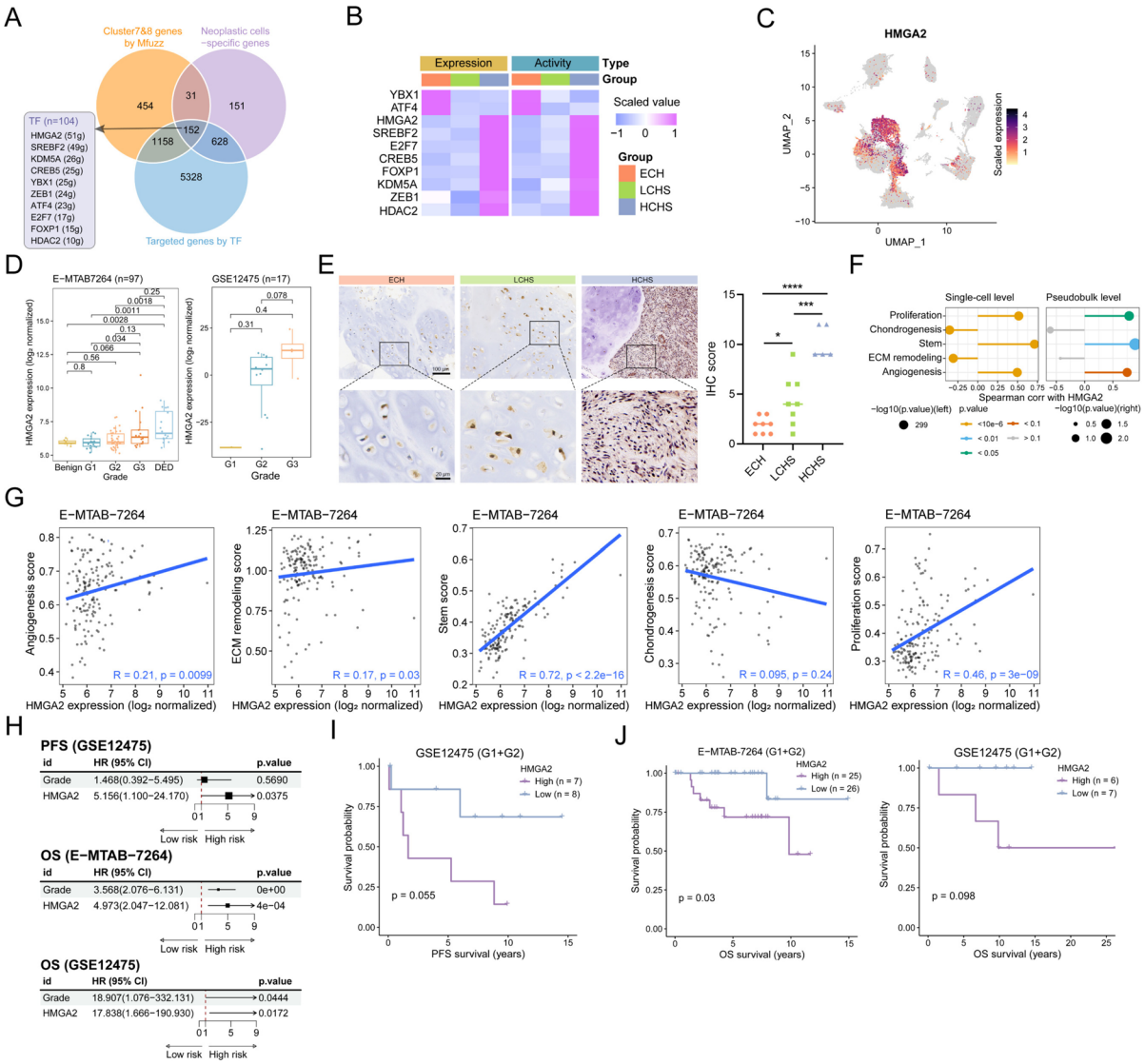

Fig. 3 HMGA2 expression patterns and clinical associations in CHS. **A** Venn diagram showing overlapping genes across groups and the transcription factors predicted to regulate these genes. **B** Heatmap showing the expression (left) and inferred regulon activity (right) of transcription factors across groups. **C** UMAP plot showing HMGA2 expression across all 11 cell types. **D** Boxplots displaying HMGA2 expression in CHS from independent cohorts. Boxes represent the interquartile range, with horizontal lines indicating the median and whiskers representing the min–max range. Statistical significance was determined by Wilcoxon tests with Benjamini–Hochberg correction. **E** Representative immunohistochemistry images (left) and quantification (right) showing HMGA2 expression in CHS from our cohort. Scale bar: 100 μm (200×) and 20 μm (400×). $*P<0.05$; $***P<0.001$; $****P<0.0001$ by one-way ANOVA with post-hoc test. **F** Lollipop plots showing Spearman correlation between HMGA2 expression and the signature scores in neoplastic cells at the single-cell level (left) and pseudobulk level (right). **G** Spearman correlation between HMGA2 expression and indicated signature scores in an independent CHS cohort. **H** Forest plot showing the independent value of HMGA2 for patient prognosis based on independent CHS cohorts. **I-J** Kaplan–Meier curves for progression-free survival (PFS) (I) and overall survival (OS) (J) in low-grade CHS patients stratified by HMGA2 expression in independent cohorts. DED, dedifferentiated

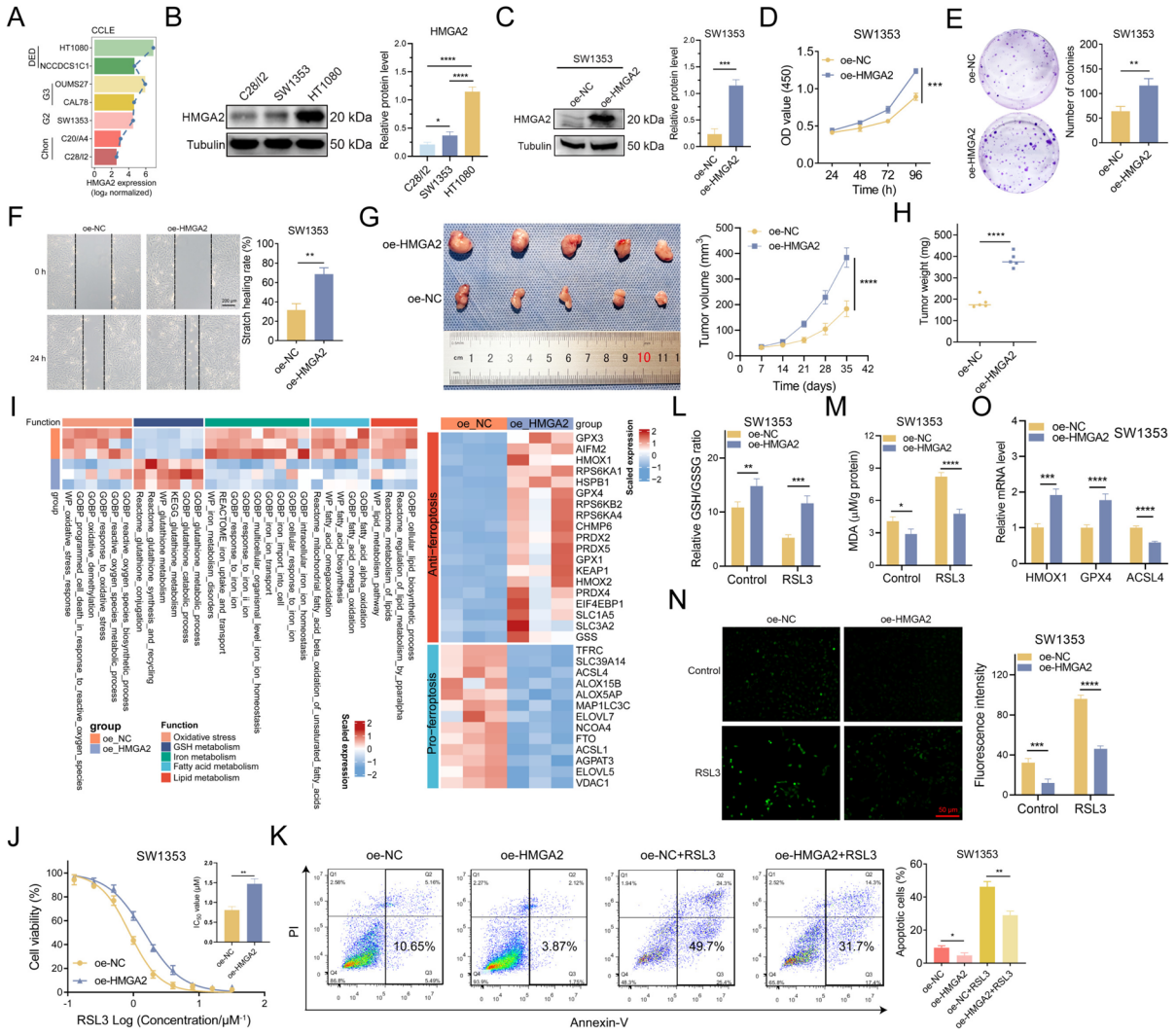

Fig. 4 HMGA2 overexpression drives malignant progression in SW1353 cells. **A** HMGA2 expression in cell lines from the Cancer Cell Line Encyclopedia (CCLE) database. **B** Representative blots (left) and densitometric quantification (right) of HMGA2 levels in the indicated cell lines. **C** Representative blots (left) and densitometric quantification (right) confirming HMGA2 overexpression efficiency. **D** Cell viability detected by CCK8 assay. **E** Representative colony images (left) and quantification (right). **F** Representative wound healing images (left) and quantification (right). Scale bar: 200 μm (200×). **G** Representative photograph (left) and tumor volume curves (right) of subcutaneous xenograft tumors. **H** Tumor weight difference at endpoint between groups. **I** Heatmap illustrating scaled signature scores (left) and ferroptosis-related gene expression (right) in groups. **J** Cell viability assessed by CCK8 assay and half-maximal inhibitory concentration (IC50) values in groups. **K** Flow-cytometry analysis (left) and quantification (right) of apoptotic cells. (L-M) GSH/GSSG ratio **L** and malondialdehyde (MDA) levels **M** across groups. **N** Representative ROS images (left) and quantified fluorescence intensities (right) across groups. Scale bar: 50 μm (200×). **O** Ferroptosis-related gene expression by RT-qPCR in groups. All error bars represent the standard deviation. $^{*}P<0.05$; $^{**}P<0.01$; $^{***}P<0.001$; $^{****}P<0.0001$ by Student's t-test (two groups) or one-way ANOVA with post-hoc test (multiple groups)

These findings suggest that HMGA2 may render low-grade CHS cells resistant to ferroptosis, thereby promoting tumor progression.

HMGA2 knockdown inhibits proliferation and sensitizes CHS cells to ferroptosis

To further elucidate the role of HMGA2 in CHS aggressiveness, we knocked it down in CHS cells (Fig. 5A, Fig. S4H and I), and assessed the consequent phenotypic changes. HMGA2 silencing significantly attenuated cell proliferation, colony-forming capacity, and migratory potential (Fig. 5B-D, Fig. S4J). In subcutaneous xenograft models, HMGA2 knockdown markedly suppressed tumor growth and reduced tumor weight (Fig. 5E and F). Notably, cells with HMGA2 knockdown were more vulnerable to RSL3-induced proliferation arrest and cell death (Fig. 5G and H, Fig. S4K). Concordantly, HMGA2-depleted cells exhibited a sharper drop in

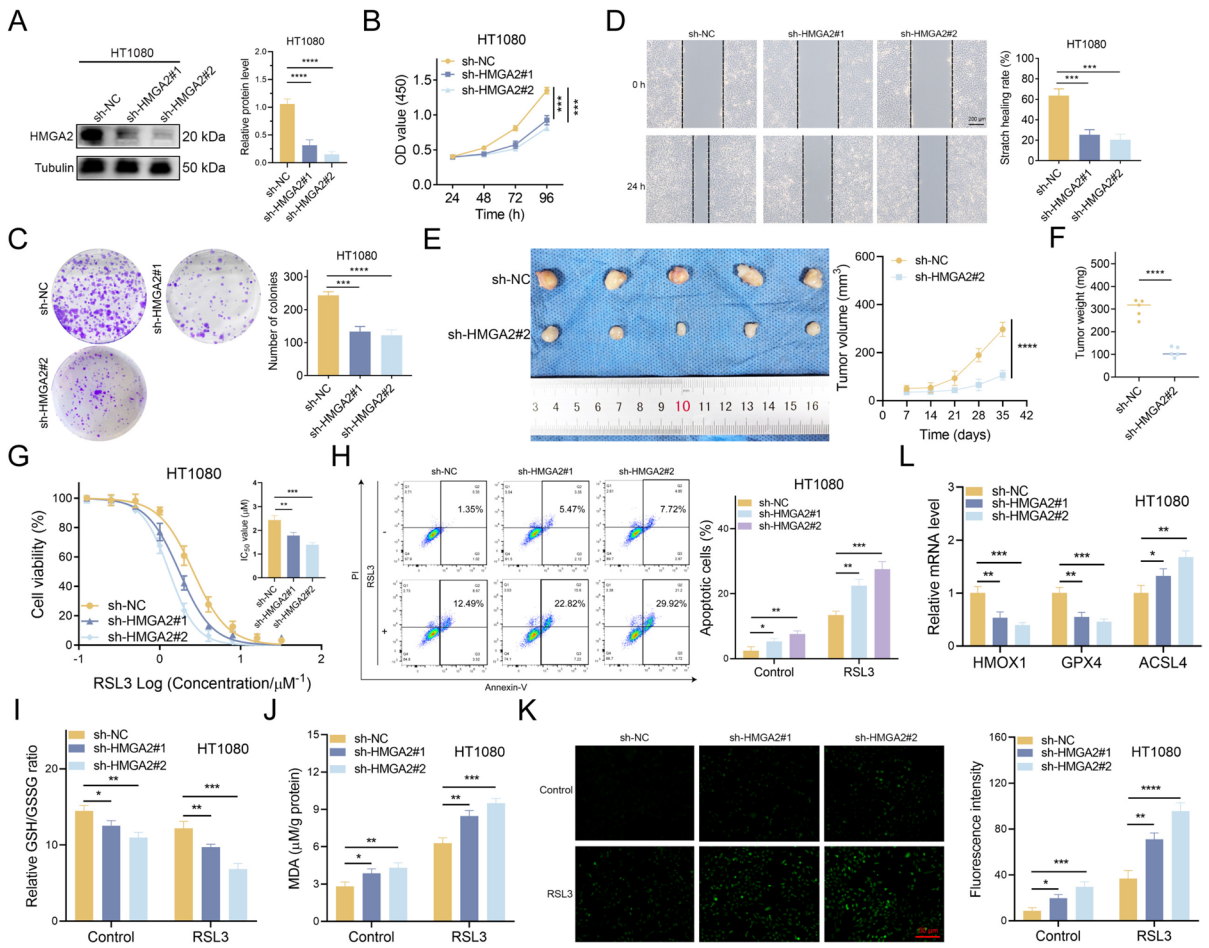

Fig. 5 HMGA2 knockdown suppresses malignant progression in HT1080 cells. **A** Representative blots (left) and densitometric quantification (right) confirming HMGA2 knockdown efficiency. **B** Cell viability detected by CCK8 assay. **C** Representative colony images (left) and quantification (right). **D** Representative wound healing images (left) and quantification (right). Scale bar: 200 μm (200×). **E** Representative photograph (left) and tumor volume curves (right) of subcutaneous xenograft tumors. **F** Tumor weight difference at endpoint between groups. **G** Cell viability assessed by CCK8 assay. **H** Flow-cytometry histograms (left) and quantification (right) of apoptotic cells. **I-J** GSH/GSSG ratio (I) and malondialdehyde (MDA) levels (J) across groups. **K** Representative fluorescence images (left) and quantification (right) of reactive oxygen species (ROS) levels across groups. Scale bar: 50 μm (200×). **L** Ferroptosis-related gene expression by RT-qPCR in groups. All error bars represent the standard deviation. $^{*}P<0.05$; $^{**}P<0.01$; $^{***}P<0.001$; $^{****}P<0.0001$ by Student's t-test (two groups) or one-way ANOVA with post-hoc test (multiple groups)

the GSH/GSSG ratio, along with greater accumulation of MDA and ROS upon RSL3 exposure, underscoring heightened ferroptosis sensitivity (Fig. 5I-K). The ferroptosis inhibitor Fer-1 partially abrogated the vulnerability conferred by HMGA2 knockdown, confirming ferroptosis specificity (Fig. S4L and M). At the molecular level, HMGA2 knockdown repressed ferroptosis suppressors (HMOX1, GPX4) while upregulating the ferroptosis driver ACSL4 (Fig. 5L). Collectively, these findings demonstrate that HMGA2 knockdown sensitizes CHS cells to ferroptosis, thereby curbing tumor progression.

Transcriptional features of endothelial cells (ECs) in CHS

Given that angiogenesis is crucial for tumor invasion in CHS (Schoedel et al. 2021), we explored the angiogenetic diversity within cartilage tumors. ECs were annotated into 6 subtypes based on canonical marker expression, namely artery ECs (AECs), capillary ECs (CapECs), vein ECs (VECs), lymphatic ECs (LECs), TipCells, and proliferating ECs (ProECs), (Fig. 6A and B, Fig. S5A-C). Among the vascular endothelial cells (VasECs), AECs, CapECs, and TipCells were categorized into tumor-associated endothelial cells (TA-ECs), while VECs were classified as tumor-associated high endothelial cells (TA-HECs) (Fig. 6C), a specialized subset implicated in immune cell trafficking within the tumor microcirculation. Enrichment analysis revealed that TA-EC-specific genes were enriched for endothelial cell migration, epithelial-mesenchymal transition, and ErbB pathway (Fig. 6D). Regarding tissue distribution, TA-ECs, exhibiting higher scores for malignant properties, were mainly enriched in HCHS (Fig. 6E and G, Fig. S5D). In contrast, VECs, which favored prognosis in CHS patients, were significantly enriched in NCHS (Fig. 6F and G, Fig. S5D). Additionally, TA-ECs derived from CHS displayed higher malignant signature scores (Fig. 6H). Collectively, these findings suggest that the transcriptional characteristics of TA-ECs in CHS may contribute to tumor aggressiveness.

Senescent phenotypes in TA-ECs of CHS

According to Mfuzz analysis in TA-ECs, genes highly expressed in CHS (clusters 1–4) were enriched for hypoxic response, oxidative stress response, and aging (Fig. 7A-B, Fig. S6A). These findings suggested that TA-ECs in CHS may acquire a senescence phenotype, which was further supported by elevated scores of multiple senescence signatures, including EC_SENESCENCE.SIG (Wu et al. 2023b), SenMayo (Saul et al. 2022), and Fridman_up (Fridman and Tainsky 2008) (Fig. 7C, Fig. S6B and C). CHS also exhibited upregulation of canonical genes linked to DNA damage response (TP53, CDKN1A, H2AFX) and the anti-apoptotic factor BCL2 (Fig. 7D). Furthermore, immunofluorescence staining confirmed robust P21 (CDKN1A) protein expression in endothelial cells within CHS tissues (Fig. 7E). Intriguingly, the senescence signature was associated with malignant characteristics (angiogenesis, extracellular matrix remodeling, and EMT) (Fig. 7F) as well as with the EGFR pathway which was elevated in CHS (Fig. 7G, Fig. S6D). EGFR activation has been reported to induce endothelial cell senescence, potentially accompanied by the secretion of senescence-associated secretory phenotype factors (Shang et al. 2020). These observations raise the possibility that cellular senescence may contribute to the malignant phenotypes of endothelial cells in CHS. Pseudotime analysis of VasECs indicated a differentiation trajectory from VECs toward Tip Cells and AECs (Fig. S7A-C), characterized by downregulation of genes associated with cell adhesion and immune cell activation (Cluster 2), alongside upregulation of genes associated with angiogenesis, hypoxia, the ErbB pathway (HBEGF), and transforming growth factor-beta response (Cluster 1) (Fig. 7H). Interestingly, we observed a positive correlation of senescence signature (EC_SENESCENCE.SIG) score with the expression of immunosuppressive genes in TA-ECs, including the cell adhesion molecule NECTIN2 (Fig. 7I), a ligand for TIGIT. Collectively, these findings indicate that endothelial cell senescence may contribute to the malignant and immunosuppressive microenvironment in CHS.

HBEGF is associated with VasEC senescence in CHS

The aforementioned results implicated EGFR pathway signaling in endothelial senescence (Fig. 7G). Given that HBEGF, an EGFR-activating ligand, has been reported to be involved in cellular senescence (Kim et al. 2021), we further explored its role in the malignant features of VasECs in CHS. HBEGF was

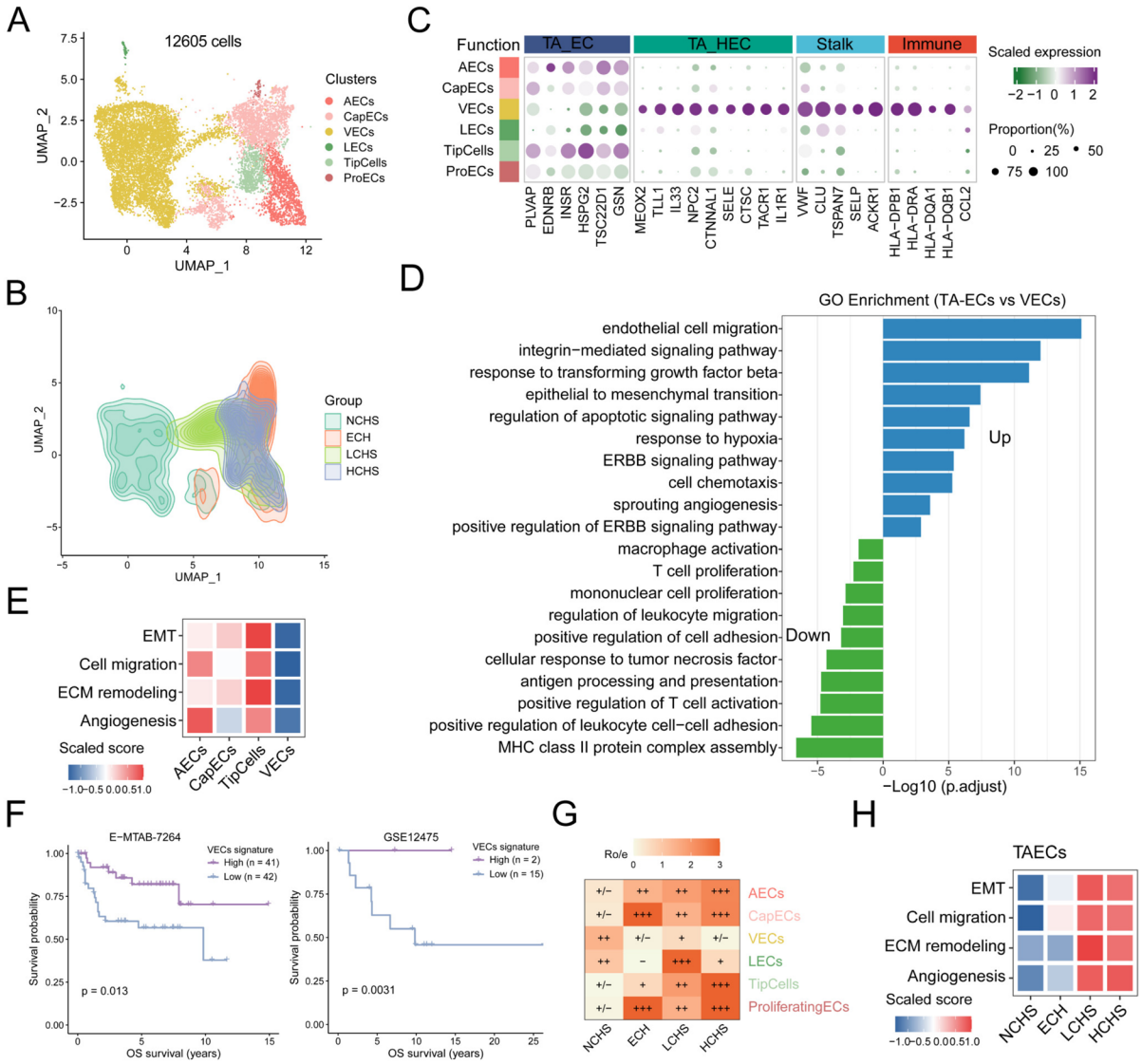

Fig. 6 Transcriptional diversity of endothelial cells in cartilage tumors. **A** UMAP plot showing the 12,605 cells annotated into 6 cell subtypes. **B** Density plot corresponding to (A) highlighting the distribution of cell subtypes across groups. **C** Dot plot showing the scaled expression of canonical marker genes in cell subtypes. **D** Bar plot showing GO enrichment analysis of differentially expressed genes between tumor-associated endothelial cells (TA-ECs) and vascular endothelial cells (VECs). **E** Heatmap displaying signature scores across vascular endothelial cells (VasECs). **F** Kaplan–Meier plots for overall survival (OS) in CHS patients stratified by VECs-signature score in independent cohorts. **G** Ro/e analysis showing the inferred relative abundance of cell subtypes. **H** Heatmap showing signature scores in TA-ECs across groups

preferentially expressed in TA-ECs (AECs, CapECs, and Tip Cells), with the highest expression observed in HCHS compared to other groups (Fig. 8A, Fig. S8A). This elevated endothelial HBEGF expression was further validated by immunohistochemical staining (Fig. 8B). We then stratified endothelial cells into HBEGF + and HBEGF- cells based on HBEGF expression (Fig. 8C). Notably, HBEGF + cells exhibited higher scores for malignancy-related signatures, and constituted a larger proportion in LCHS and HCHS (Fig. S8B and C). Differential gene expression analysis indicated that HBEGF + cells highly expressed TA-EC-related genes (EDNRB, TSC22D1, INSR, HSPG2, GSN) (Fig. S8D). Enrichment

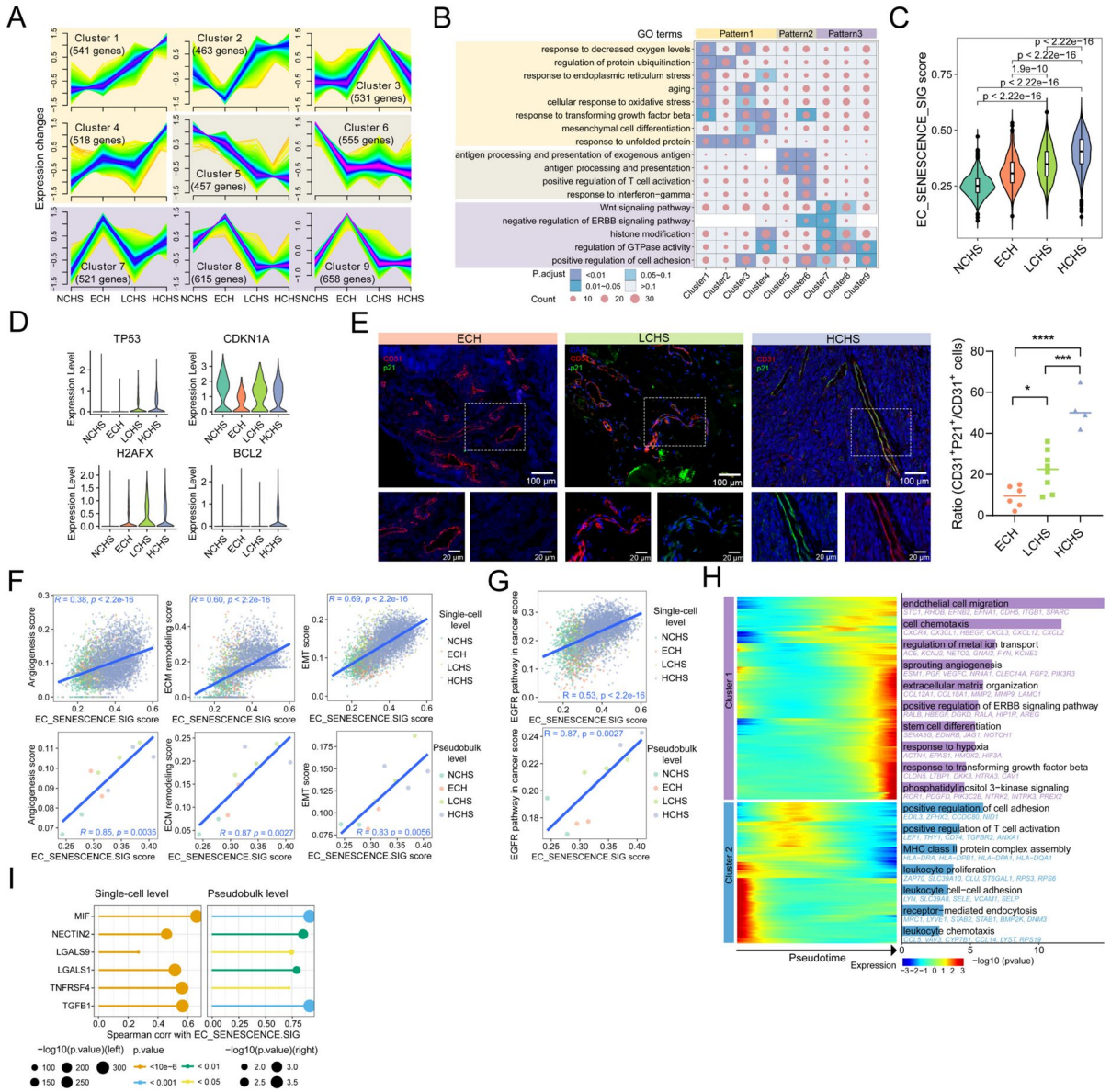

Fig. 7 Senescence characteristics of tumor-associated endothelial cells in CHS. **A** Mfuzz clustering analysis identifying genes with dynamic expression patterns in endothelial cells across groups. **B** Heatmap showing GO enrichment analysis of genes from each Mfuzz cluster identified in (A). **C** Violin-box plot displaying senescence-related signature score across groups. Boxes represent the interquartile range, with horizontal lines indicating the median and whiskers representing the min–max range. Statistical significance was determined by Wilcoxon tests with Benjamini–Hochberg correction. **D** Violin plots showing expression levels of senescence-related genes across groups. **E** Representative immunofluorescence images (left) and quantification (right) of p21 expression across groups. Scale bar: 100 μm (200×) and 20 μm (400×). $^{*}P<0.05$; $^{***}P<0.001$; $^{****}P<0.0001$ by one-way ANOVA with post-hoc test. **F** Spearman correlation between signature scores in tumor-associated endothelial cells (TA-ECs) at the single-cell level (upper) and pseudobulk level (lower). **G** Spearman correlation between EC_SENESCENCE.SIG and EGFR pathway signature scores in TA-ECs at the single-cell level (upper) and pseudobulk level (lower). **H** Expression dynamics of representative genes (left) along the inferred pseudotime trajectory and the GO enrichment (right). **I** Lollipop plots showing Spearman correlation between EC_SENESCENCE.SIG and immunosuppressive markers at the single-cell level (left) and pseudobulk level (right) in TA-ECs

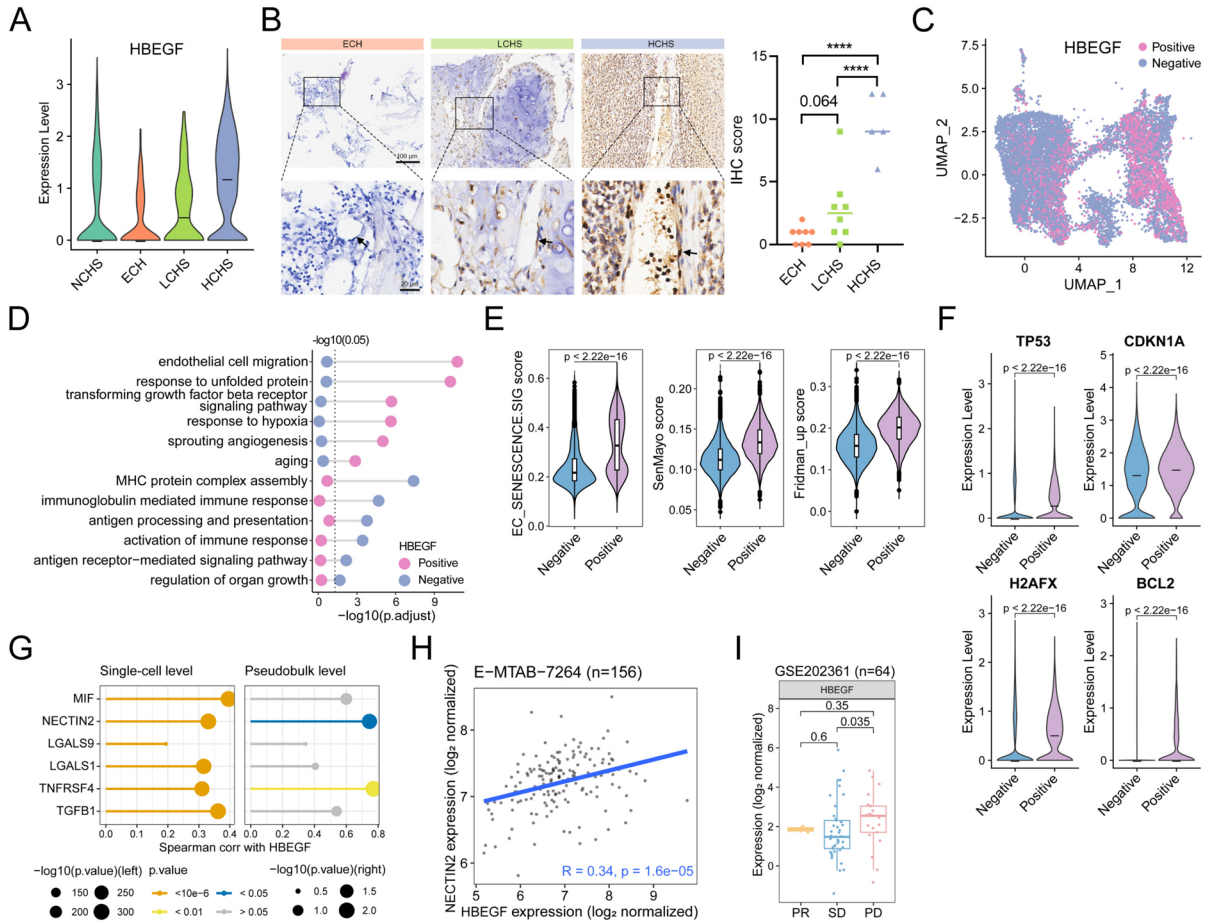

Fig. 8 HBEGF association with endothelial cell senescence in CHS. **A** Violin plot showing HBEGF expression across groups in tumor-associated endothelial cells (TA-ECs). **B** Representative immunohistochemistry images (left) and quantification of HBEGF staining scores (right) in endothelial cells (black arrows) across groups. Scale bar: 100 μm (200×) and 20 μm (400×). ****$P < 0.0001$ by one-way ANOVA with post-hoc test. **C** UMAP plot of endothelial cells colored by HBEGF expression status. **D** Lollipop plot showing GO enrichment analysis of differentially expressed genes between HBEGF-positive and -negative cells. **E** Violin-box plots comparing senescence-signature scores between HBEGF-positive and HBEGF-negative cells. **F** Violin plots showing senescence-related gene expression in HBEGF-positive and -negative cells, with horizontal lines indicating median values. **G** Lollipop plots illustrating Spearman correlation between HBEGF and immunosuppressive markers in endothelial cells at the single-cell level (left) and pseudobulk level (right). **H** Spearman correlation between HBEGF and NECTIN2 expression in CHS from an independent cohort. **I** Boxplot showing HBEGF expression in an independent sarcoma cohort receiving immunotherapy. PR: partial response; SD: stable disease; PD: progressive disease. Boxes represent the interquartile range, with horizontal lines indicating the median and whiskers representing the min–max range. Statistical significance (E, F and I) was determined by Wilcoxon tests with Benjamini–Hochberg correction

analysis further revealed that genes upregulated in HBEGF + cells were related to angiogenesis and aging, while the downregulated ones were associated with immune activation (Fig. 8D). The senescence phenotype of HBEGF + cells was supported by elevated senescence-signature scores and increased expression of canonical senescence markers (Fig. 8E and F). The correlation between HBEGF expression and malignant or senescent features was confirmed in an independent public CHS cohort (Fig. S8E). Pseudotime trajectory analysis positioned HBEGF + cells predominantly at the terminal ends, suggesting their transition toward cellular senescence during CHS progression (Fig. S8F and G). Accordingly, the

EGFR pathway, known to be linked to senescence, was found to be activated in HBEGF + cells (Fig. S8H). Notably, HBEGF expression showed a significant correlation with NECTIN2, a molecule specifically expressed in endothelial cells (Fig. 8G and H, Fig. S8I). Furthermore, HBEGF expression was elevated in sarcoma patients exhibiting disease progression following immunotherapy (Fig. 8I). Collectively, these findings indicated that HBEGF may serve as a critical factor in VasECs within CHS, potentially promoting cellular senescence and immunosuppression, thereby contributing to tumor progression.

Cellular interactions between neoplastic cells and TA-ECs in CHS

To decipher the intercellular crosstalk within the CHS microenvironment, we utilized CellChat to infer interactions between neoplastic cells and TA-ECs. Overall communication intensity was higher in HCHS than in LCHS (Fig. 9A). Notably, neoplastic cells in HCHS engaged in both more numerous and stronger interactions with all three TA-EC clusters compared to those in LCHS (Fig. 9B). LCHS was characterized by abundant THBS and APP signaling, along with a uniquely prominent CCL signal. In contrast, HCHS exhibited intense COLLAGEN and LAMININ signaling, with SPP1 emerging as the most distinctive pathway (Fig. 9C). Ligand-receptor pair analysis revealed that HCHS displayed robust interactions with TA-ECs via SPP1 paired with ITGA5_ITGB1, ITGA8_ITGB1, and ITGA9_ITGB1, which were absent in LCHS (Fig. 9D). Inferred signaling flow suggested that SPP1 originated from neoplastic cells (senders) and primarily targeted AECs, CapECs, and TipCells (receivers) (Fig. 9E). Among the identified pairs, SPP1-ITGA5_ITGB1 emerged as the dominant mediator of SPP1 signaling from neoplastic cells to TA-ECs, with both ligand and receptors demonstrating elevated expressions in HCHS (Fig. 9F and G). Additionally, high SPP1 expression was associated with unfavorable prognosis in patients with CHS or sarcoma (Fig. 9H). Intriguingly, communications from TA-ECs to neoplastic cells through the HBEGF-EGFR pair, a representative component of the EGF pathway, were also more frequent in HCHS (Fig. 9D). In this pathway, TA-ECs functioned as senders, while neoplastic cells acted as receivers (Fig. 9I). Both HBEGF and EGFR, key components of EGF signaling, exhibited elevated expression levels in HCHS (Fig. 9J and K). Moreover, elevated HBEGF expression correlated with shorter survival in patients with CHS or sarcoma (Fig. 9L). Collectively, these findings suggest that SPP1- and EGF-mediated crosstalk between neoplastic cells and TA-ECs may contribute to the invasive phenotype of CHS.

HMGA2 promotes endothelial senescence via SPP1-ITGA5_ITGB1 signaling in CHS

To investigate whether HMGA2 contributes to endothelial cell senescence by regulating SPP1, we examined the effect of HMGA2 modulation on SPP1 levels in CHS cells. HMGA2 overexpression in SW1353 cells markedly upregulated SPP1 transcription and secretion, whereas its knockdown in HT1080 cells suppressed both intracellular and secreted SPP1 levels (Fig. 10A-B). We then treated HUVEC cells with conditioned medium from CHS cells (Fig. 10C). Exposure to medium from oe-HMGA2 SW1353 cells increased the fraction of SA-β-gal-positive HUVEC cells, whereas medium from sh-HMGA2 HT1080 cells decreased it, compared to the respective controls (Fig. 10D). These HMGA2-driven effects were dependent on SPP1, as an SPP1 inhibitor abolished the increase induced by oe-HMGA2 medium, and recombinant SPP1 restored the decrease caused by sh-HMGA2 medium (Fig. 10D). To functionally validate ITGA5_ITGB1 as a key mediator of SPP1-driven senescence, we employed ATN-161, a selective α5β1 integrin inhibitor. In SW1353 cells, ATN-161 treatment significantly reduced the SA-β-gal-positive fraction of HUVECs cultured with oe-HMGA2 conditioned medium, while exerting minimal effect on the oe-NC group (Fig. S9A). Similarly, in HT1080 cells, ATN-161 markedly decreased endothelial senescence in the sh-NC group, but showed negligible impact in the sh-HMGA2 group (Fig. S9B). Collectively, these results demonstrate that the SPP1-ITGA5_ITGB1 signaling axis mediates HMGA2-induced endothelial senescence. Interestingly, HMGA2 and HBEGF expression showed a positive correlation in CHS and sarcoma cohorts (Fig. 10E), which was validated by immunohistochemical staining in our cohort (Fig. 10F). Additionally, HUVEC cells secreted more HBEGF when exposed to conditioned medium from oe-HMGA2 SW1353 cells and less when exposed to medium from sh-HMGA2 HT1080 cells, relative to their respective controls (Fig. 10G). Therefore, these findings uncovered that HMGA2 in CHS cells may

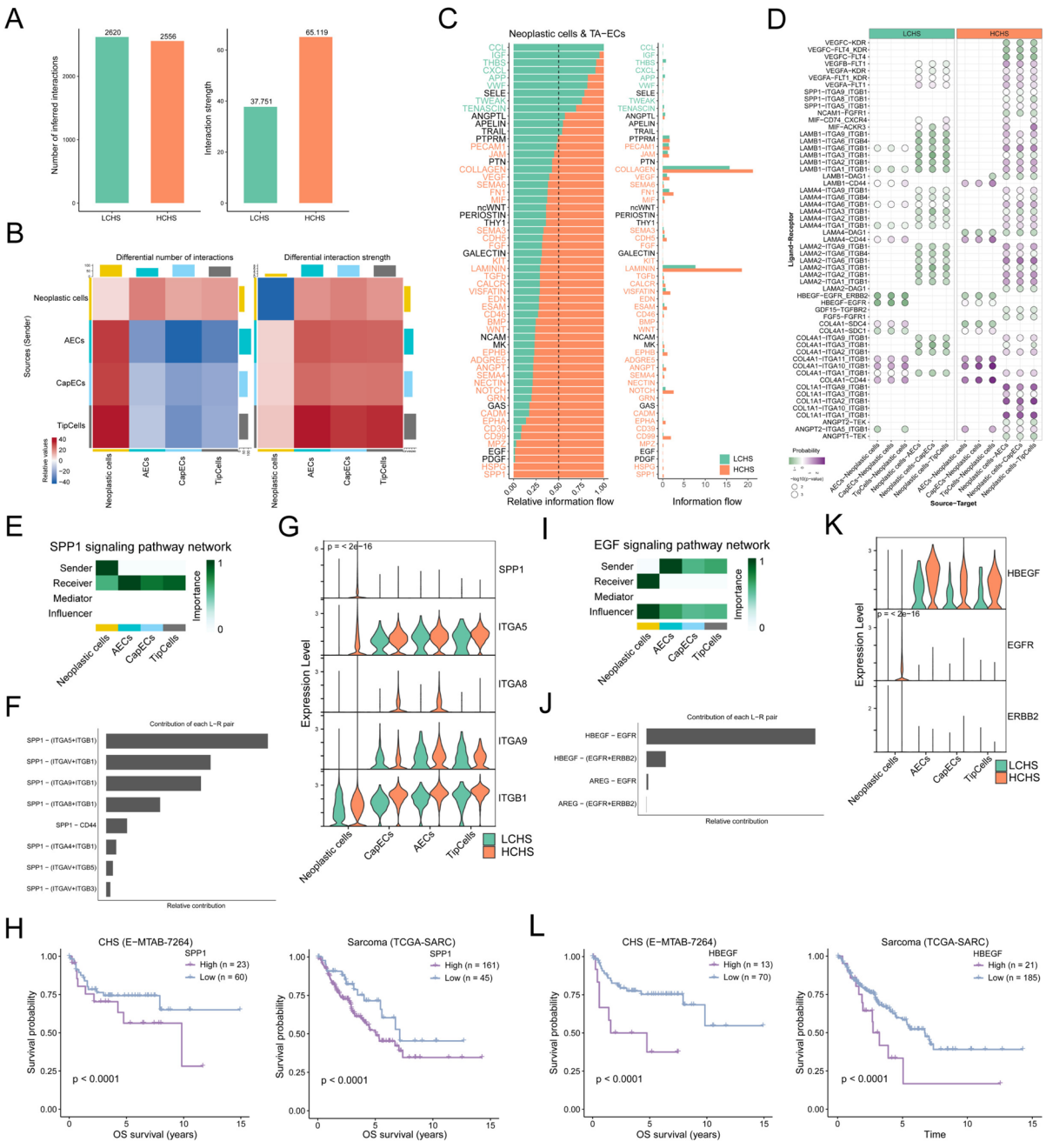

promote endothelial senescence through the SPP1-ITGA5_ITGB1 signaling axis.

Discussion

Chondrosarcoma (CHS) is an uncommon mesenchymal neoplasm. Considering the scant benefit of adjuvant therapy for high-grade CHS (Tlemsani et al. 2023), alternative treatment targets are required to improve the clinical outcome of these patients. Here, we deciphered the profile variety of neoplastic and endothelial cells in ECH, LCHS and HCHS. Neoplastic cells demonstrated aggravated proliferation and angiogenesis characteristics in CHS progression, with HMGA2 promoting tumor malignancy and

◂**Fig. 9** Cellular interactions between neoplastic cells and tumor-associated endothelial cells (TA-ECs) inferred by Cellchat. **A** Bar plots showing the number (left) and interaction strength (right) of inferred cell–cell communications between neoplastic cells and TA-ECs. **B** Interaction number (left) and strength (right) in HCHS versus LCHS groups. **C** Bar plots showing the relative (left) and overall (right) information flow of signaling pathways mediating communication between neoplastic cells and TA-ECs. **D** Dot plot displaying significant ligand-receptor pairs inducing interactions between neoplastic cells and TA-ECs. **E** Functional roles of cell clusters within the SPP1 pathway. **F** Bar plot showing the relative contributions of individual ligand-receptor pairs to the overall SPP1 signaling pathway. **G** Violin plots showing the expression levels of SPP1 ligand and its cognate receptors. **H** Kaplan–Meier plots comparing overall survival (OS) between patients with high versus low SPP1 expression in independent cohorts. **I** Functional roles of cell clusters within the EGF pathway. **J** Bar plot showing the relative contributions of individual ligand-receptor pairs to the overall EGF pathway. **K** Violin plots showing the expression levels of EGF ligand and its receptors. **L** Kaplan–Meier plots comparing overall survival (OS) between patients with high versus low HBEGF expression in independent cohorts. Statistical significance was determined by Wilcoxon tests with Benjamini–Hochberg correction

predicting unfavorable outcome of CHS patients. The TA-ECs presented senescent characteristics in CHS, which were related to HBEGF. Additionally, HCHS presented more prevalent cellular communications between neoplastic cells and TA-ECs mediated by SPP1 and EGF pathways. HMGA2-SPP1 axis in neoplastic cells induced senescence in endothelial cells, accompanied by HBEGF secretion (Fig. 11).

A recent study linked endoplasmic reticulum stress to malignant transformation from benign tumor to CHS (Su et al. 2024). Our single-cell atlas identified higher proliferative and angiogenetic abilities in neoplastic cells along the malignant progression of CHS, with the pro-proliferation signatures predicting poor patient outcome. The study by Chirico et al. demonstrated that elevated HMGA2 immunostaining was associated with invasive tumor growth, advanced stage and metastasis (Chirico et al. 2025). In malignant peripheral nerve sheath tumors, HMGA2-positive patients were also found to suffer shorter survival than HMGA2-negative patients (Yang et al. 2019). According to a meta-analysis, high HMGA2 level was associated with poor overall survival in patients with several carcinomas (Huang et al. 2018). However, HMGA2 implication in CHS remains unclear. Our study observed progressively more intensive HMGA2 expression in LCHS and HCHS. Moreover, HMGA2 expression in neoplastic cells was associated with proliferation and angiogenesis, and indicated unfavorable prognosis for CHS patients. Activation of antiapoptotic pathways, ROS catabolism-related DNA damage protection contribute to the chemo- and radio-resistance in CHS (Gilbert et al. 2023). Wu et al. observed highly activated glutamine metabolism and low ROS accumulation in cisplatin-resistant CHS cells, indicating ferroptosis involvement (Wu et al. 2023a). Our study revealed that HMGA2 promoted cell proliferation, cell migration, tumor growth, accompanied by ferroptosis defense in CHS cells. Similarly, Luo et al. reported HMGA2 contribution to ferroptosis defense in pancreatic cancer cells (Luo et al. 2024). Therefore, therapy targeting HMGA2 may aid in disease control in CHS.

Despite the origin from avascular cartilage, emerging evidence has shown microvascularity in CHS tissues, which contributes to aggressive clinical behavior and an increased potential for metastasis (Tlemsani et al. 2023). Pazopanib, a multitargeted tyrosine kinase inhibitor with antiangiogenic activity represents positive effects for patients with surgically unresectable or metastatic CHS in a clinical study (Chow et al. 2020). Combined approaches of chemotherapy with antiangiogenic agents for advanced CHS are also in development in clinical trials (Ingangi et al. 2024). However, the endothelial microenvironment in CHS has not been fully elucidated, limiting more options for antiangiogenic agents. We exploited the endothelial cells in CHS at single-cell resolution, revealing a senescent feature in the tumor-infiltrated endothelial cells, with HBEGF as a responsible target. Additionally, we found an association of cellular senescence with aggravated angiogenesis and endothelial-mesenchymal transition, which were consistent with our recent study (Wang et al. 2024) as well as the study by Benadjaoud et al. (Benadjaoud et al. 2022). Mechanistically, senescent cells may promote tumor angiogenesis by secreting high levels of SASP factors, including VEGF, PDGF, and FGF (Xiong et al. 2024). HBEGF was recently regarded as a senescence associated gene (Li et al. 2024). In TNBC, HBEGF activates the tube formation of endothelial cells to support tumor aggressiveness (Yotsumoto et al. 2013). Additionally, cellular senescence in the tumor microenvironment is able to induce immunosuppression (Takasugi et al. 2022; Wang et al. 2024). We observed higher expression

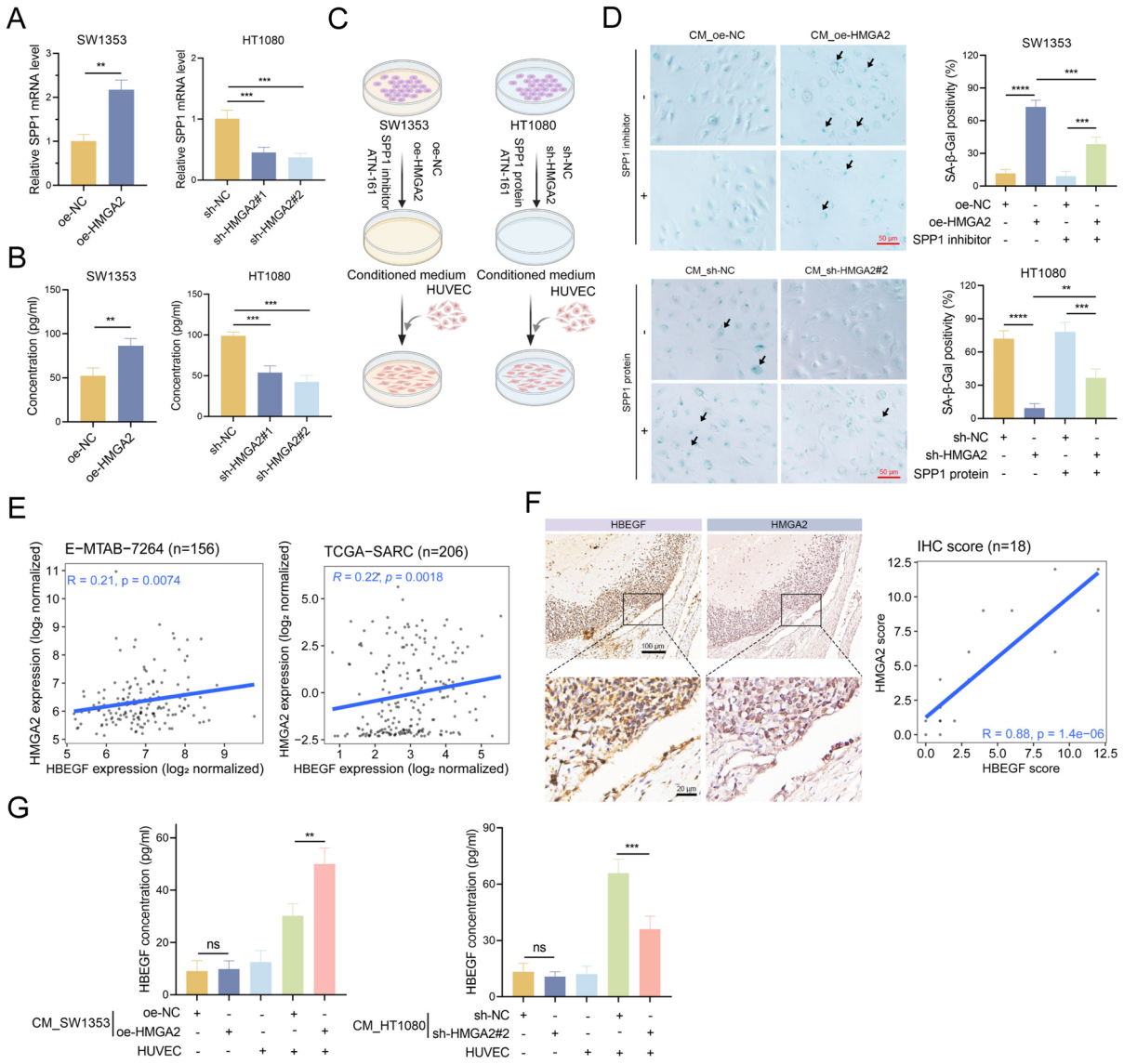

Fig. 10 HMGA2 drives endothelial senescence through the SPP1 pathway in CHS. **A** SPP1 mRNA levels determined by RT-qPCR in CHS cells. **B** SPP1 protein levels secreted by CHS cells determined by ELISA. **C** Schematic diagram depicting HUVEC cells cultured in conditioned medium collected from CHS cells. **D** Representative images (left) and quantification (right) of SA-β-gal-positive (black arrow) HUVECs cultured in conditioned medium from CHS cells. Scale bar: 50 μm (200×). **E** Spearman correlation between HBEGF and HMGA2 expressions from independent cohorts. **F** Representative immunohistochemistry images showing co-expression of HBEGF and HMGA2 in a single CHS specimen (left) and Spearman correlation analysis of their staining scores (right). Scale bar: 100 μm (200×) and 20 μm (400×). **G** HBEGF protein levels secreted by HUVEC cells determined by ELISA. CM, conditioned medium. All error bars represent the standard deviation. ns, not significant; $^{**}P<0.01$; $^{***}P<0.001$; $^{****}P<0.0001$ by one-way ANOVA with post-hoc test

of HBEGF in the dedifferentiated sarcoma patients with poor response to immune checkpoint blockade. Specifically, HBEGF was associated with NECTIN2, an exclusively expressed gene in endothelial cells in CHS. NECTIN2_TIGIT pair has been characterized as inactivators of T and NK cell activity (Xu et al. 2024). According to a recent study by Agorku et al., NECTIN2 expressed by CAF was a crucial regulator of $CD8^{+}$T cell exhaustion (Agorku et al. 2024). Therefore, HBEGF may serve as a critical target to

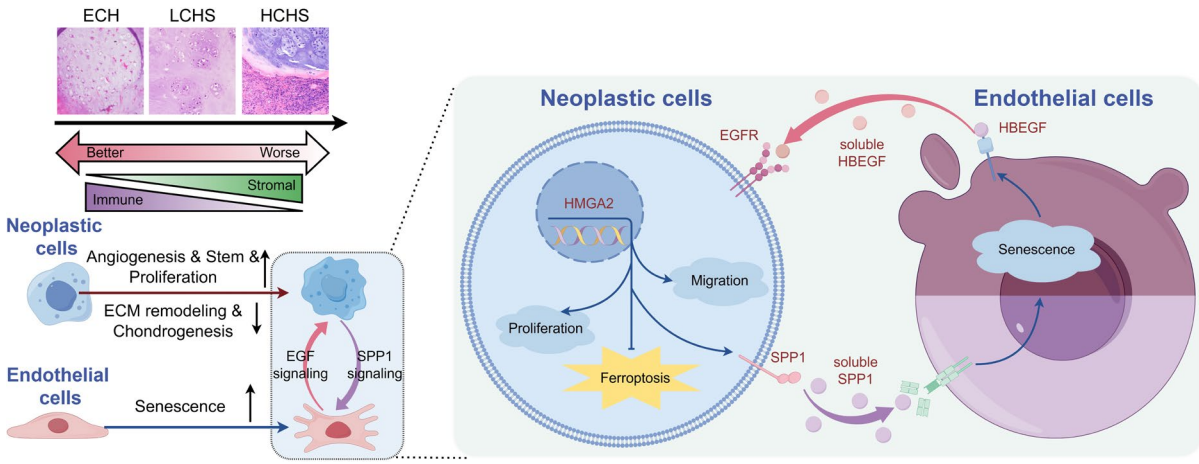

Fig. 11 Schematic diagram depicting the transcriptional heterogeneity in neoplastic and endothelial cells across ECH, LCHS, and LCHS, and their intercellular crosstalk. ECH, enchondroma; LCHS, low-grade chondrosarcoma; HCHS, high-grade chondrosarcoma. This figure was created by Figdraw platform

reserve endothelial senescence and to improve the efficacy for anti-angiogenesis in CHS.

In this study, cellular communications between tumor cells and TA-ECs was uncovered. In HCHS, we found that tumor cells signal to TA-ECs through SPP1 signaling, and TA-ECs signal back to tumor cells through EGF signaling, forging a paracrine loop. Several studies have shown that CHS cells promote angiogenesis in a vascular endothelial growth factor-dependent manner (Chen et al. 2019; Lin et al. 2014; Wu et al. 2014). However, whether the HMGA2-SPP1 axis regulates endothelial senescence in CHS has not been explored. According to a recent study, SPP1 is markedly up-regulated in late-stage pancreatic cancer. Genetic ablation of SPP1 postpones tumor initiation and prevents metastatic spread (Li et al. 2025). A recent study by Gu et al. reported that SPP1 induces nucleus pulposus cell senescence via inhibiting mitophagy (Gu et al. 2025). In osteoarthritic cartilage, SPP1-positive chondrocytes display heightened angiogenesis capacity and pronounced senescent characteristics (Qu et al. 2023). SPP1 is also identified as a senescence marker for vascular cells (Mazan-Mamczarz et al. 2025). SPP1 knockdown suppresses the senescence-associated secretory phenotype via reducing p53 activation (Yuan et al. 2025). As a secreted signaling molecule, SPP1 also orchestrates intercellular communication that fuels tumor evolution. In colorectal cancer, tumor cell-derived SPP1 stimulates CXCL12 production from cancer-associated fibroblasts to support immunotherapeutic resistance and liver metastasis (Liu et al. 2025). In endometrial carcinoma, tumor cells release SPP1 to promote the proliferation, invasion and migration of tumor cells and angiogenesis of endothelial cells (Ma et al. 2024). Our recent study demonstrated that SPP1 derived from malignant cells contributes to the senescence of vascular endothelial cells and a pro-angiogenic microenvironment that favors lung cancer bone metastasis (Wang et al. 2024). In CHS, elevated SPP1 levels have been found to correlate with high tumor grade and metastasis (Nazarizadeh et al. 2021). In this study, we observed that SPP1 secreted by HMGA2-overexpressing CHS cells activates the ITGA5_ITGB1 axis in endothelial cells, driving endothelial senescence and subsequent HBEGF secretion. This establishes SPP1 as an upstream regulator of HBEGF via endothelial senescence. Thus, the HMGA2-SPP1 axis may contribute to endothelial senescence in CHS, representing a potential therapeutic target.

Several limitations should be noted in this study. Since the sample size of HCHS cases was small with histologically heterogeneity, our transcriptomic findings warrant validation in larger multi-center cohorts. Additionally, while CellChat analysis identified potential HBEGF-EGFR crosstalk between tumor-associated endothelial cells and neoplastic cells, the downstream oncogenic mechanisms remain to be fully elucidated.

Conclusions

In conclusion, this study deciphered the transcriptional characteristics of neoplastic and endothelial cells in CHS by scRNA-seq. HMGA2 in neoplastic cells was identified as a vital regulator for the malignant properties in CHS. TA-ECs in CHS underwent senescence phenotypes which were associated with HBEGF. Additionally, our findings revealed the intratumoral interactions between neoplastic cells and TA-ECs induced by HMGA2-mediated SPP1 pathway, offering new insights into the mechanisms underlying the senescent endothelial microenvironment in CHS. While further functional validation is warranted, this study contributes to a deeper understanding of features of CHS progression and provides potential targets for the precise treatment of advanced disease.

Acknowledgements The illustrating images were accomplished on the Figdraw platform.

Author contributions S.W. and S.L. drafted the manuscript; X.W. and H.W. collected the samples and conducted the experiments; H.Z., W.Z. and J.L. provided bioinformatics support; X.H., F.L. and Z.W. generated the figures and tables; J.L., X.S., and L.A. reviewed the manuscript and made significant revisions. The final manuscript has been approved by all authors.

Funding This study was supported by the Natural Science Foundation of Fujian Province (grant number 2025J0132), the Joint Funds for the Innovation of Science and Technology, Fujian province (grant number 2024Y9414).

Data availability Human scRNA-seq data have been uploaded to the Genome Sequence Archive (GSA) of the National Genomics Data Center (https://ngdc.cncb.ac.cn/gsa/) under accession code HRA009334. The transcriptomic sequencing data of SW1353 cells have been uploaded to the Gene Expression Omnibus (https://www.ncbi.nlm.nih.gov/geo/) under accession code GSE289237. Publicly available datasets utilized in this study can be found here: E-MTAB-7264 at https://www.ebi.ac.uk/arrayexpress, GSE12475 and GSE202361 at https://www.ncbi.nlm.nih.gov/geo/. The codes for data analysis and figure generation are available from the corresponding author (Lu Ao) upon reasonable request.

Declarations

Ethics approval and consent to participate The research complied with the Declaration of Helsinki and the protocols involving human samples were approved by the Ethics Committee of the First Affiliated Hospital of Fujian Medical University. All participants provided written informed consent. The in vivo experiments using nude mice was approved by the Ethics Review Committee of Fujian Medical University.

Competing interests The authors declare no competing interests.

References

Agorku DJ, Bosio A, Alves F, et al. Colorectal cancer-associated fibroblasts inhibit effector T cells via NECTIN2 signaling. Cancer Lett. 2024;595:216985.

Aibar S, González-Blas CB, Moerman T, et al. SCENIC: single-cell regulatory network inference and clustering. Nat Methods. 2017;14(11):1083–6.

Andreatta M, Carmona SJ. UCell: Robust and scalable single-cell gene signature scoring. Comput Struct Biotechnol J. 2021;19:3796–8.

Baslan T, Hicks J. Unravelling biology and shifting paradigms in cancer with single-cell sequencing. Nat Rev Cancer. 2017;17(9):557–69.

Benadjaoud MA, Soysouvanh F, Tarlet G, et al. Deciphering the dynamic molecular program of radiation-induced endothelial senescence. Int J Radiat Oncol Biol Phys. 2022;112(4):975–85.

Butler A, Hoffman P, Smibert P, et al. Integrating single-cell transcriptomic data across different conditions, technologies, and species. Nat Biotechnol. 2018;36(5):411–20.

Chen SS, Tang CH, Chie MJ, et al. Resistin facilitates VEGF-A-dependent angiogenesis by inhibiting miR-16-5p in human chondrosarcoma cells. Cell Death Dis. 2019;10(1):31.

Chirico V, Ergüven FB, Möller K, et al. High mobility group protein 2 (HMGA2) is highly expressed in a broad range of benign and malignant tumors. Virchows Arch. 2025;487(1):183–201.

Chow WA. Chondrosarcoma: biology, genetics, and epigenetics. F1000Res. 2018;7:F1000 Faculty Rev-1826.

Chow W, Frankel P, Ruel C, et al. Results of a prospective phase 2 study of pazopanib in patients with surgically unresectable or metastatic chondrosarcoma. Cancer. 2020;126(1):105–11.

Fridman AL, Tainsky MA. Critical pathways in cellular senescence and immortalization revealed by gene expression profiling. Oncogene. 2008;27(46):5975–87.

Gilbert A, Tudor M, Montanari J, et al. Chondrosarcoma resistance to radiation therapy: origins and potential therapeutic solutions. Cancers (Basel). 2023;15(7):1962.

Gordon S, Martinez FO. Alternative activation of macrophages: mechanism and functions. Immunity. 2010;32(5):593–604.

Gu H, Li Q, Liu Z, et al. SPP1-ITGα5/β1 accelerates calcification of nucleus pulposus cells by inhibiting mitophagy via ubiquitin-dependent PINK1/PARKIN pathway blockade. Adv Sci. 2025;12(7):e2411162.

Hu J, Zhang L, Xia H, et al. Tumor microenvironment remodeling after neoadjuvant immunotherapy in non-small cell lung cancer revealed by single-cell RNA sequencing. Genome Med. 2023;15(1):14.

Huang B, Yang J, Cheng Q, et al. Prognostic value of HMGA2 in human cancers: a meta-analysis based on literatures and TCGA datasets. Front Physiol. 2018;9:776.

Ingangi V, De Chiara A, Ferrara G, et al. Emerging treatments targeting the tumor microenvironment for advanced chondrosarcoma. Cells. 2024;13(11):977.

Jin S, Guerrero-Juarez CF, Zhang L, et al. Inference and analysis of cell-cell communication using CellChat. Nat Commun. 2021;12(1):1088.

Kim H, Cho Y, Kim HS, et al. A system-level approach identifies HIF-2α as a critical regulator of chondrosarcoma progression. Nat Commun. 2020;11(1):5023.

Kim SR, Puranik AS, Jiang K, et al. Progressive cellular senescence mediates renal dysfunction in ischemic nephropathy. J Am Soc Nephrol. 2021;32(8):1987–2004.

Korsunsky I, Millard N, Fan J, et al. Fast, sensitive and accurate integration of single-cell data with Harmony. Nat Methods. 2019;16(12):1289–96.

Li B, Li G, Yan X, et al. Fresh tissue multi-omics profiling reveals immune classification and suggests immunotherapy candidates for conventional chondrosarcoma. Clin Cancer Res. 2021;27(23):6543–58.

Li J, Jiang S, Huang C, et al. Identification and validation of genes associated with aging-related cardiovascular disease. FASEB J. 2024;38(1):e23370.

Li H, Lan L, Chen H, et al. SPP1 is required for maintaining mesenchymal cell fate in pancreatic cancer. Nature. 2025;648(8092):203–9.

Lin CY, Hung SY, Chen HT, et al. Brain-derived neurotrophic factor increases vascular endothelial growth factor expression and enhances angiogenesis in human chondrosarcoma cells. Biochem Pharmacol. 2014;91(4):522–33.

Liu S, Zhang Z, Wang Z, et al. SPP1 drives colorectal cancer liver metastasis and immunotherapy resistance by stimulating CXCL12 production in cancer-associated fibroblasts. Cancer Res. 2025;86(1):58–79.

Luo Z, Zheng Q, Ye S, et al. HMGA2 alleviates ferroptosis by promoting GPX4 expression in pancreatic cancer cells. Cell Death Dis. 2024;15(3):220.

Ma H, Weng F, Tong X, et al. LncRNA TRPM2-AS promotes endometrial carcinoma progression and angiogenesis via targeting miR-497-5p/SPP1 axis. Cell Mol Biol Lett. 2024;29(1):93.

MacDonald IJ, Lin CY, Kuo SJ, et al. An update on current and future treatment options for chondrosarcoma. Expert Rev Anticancer Ther. 2019;19(9):773–86.

Mazan-Mamczarz K, Tsitsipatis D, Childs BG, et al. Single-cell and spatial transcriptomics map senescent vascular cells in arterial remodeling during atherosclerosis in mice. Nat Aging. 2025;5(8):1528–47.

McGinnis CS, Murrow LM, Gartner ZJ. DoubletFinder: doublet detection in single-cell RNA sequencing data using artificial nearest neighbors. Cell Syst. 2019;8(4):329-337.e4.

Nakagawa M, Shimada E, Guardino N, et al. Protein phosphatase 1 regulatory subunit 3C integrates cholesterol metabolism and isocitrate dehydrogenase in chondrocytes and neoplasia. Proc Natl Acad Sci U S A. 2025;122(16):e2501519122.

Nazarizadeh A, Alizadeh-Fanalou S, Hosseini A, et al. Evaluation of local and circulating osteopontin in malignant and benign primary bone tumors. J Bone Oncol. 2021;29:100377.

Patel AP, Tirosh I, Trombetta JJ, et al. Single-cell RNA-seq highlights intratumoral heterogeneity in primary glioblastoma. Science. 2014;344(6190):1396–401.

Qiu X, Mao Q, Tang Y, et al. Reversed graph embedding resolves complex single-cell trajectories. Nat Methods. 2017;14(10):979–82.

Qu Y, Wang Y, Wang S, et al. A comprehensive analysis of single-cell RNA transcriptome reveals unique SPP1+ chondrocytes in human osteoarthritis. Comput Biol Med. 2023;160:106926.

Saul D, Kosinsky RL, Atkinson EJ, et al. A new gene set identifies senescent cells and predicts senescence-associated pathways across tissues. Nat Commun. 2022;13(1):4827.

Schoedel K, Miller V, Osei-Hwedieh D, et al. Differential expression of angiogenesis markers HSP70, HSP90, VEGF and pERK1/2 in both components of dedifferentiated chondrosarcomas. J Bone Oncol. 2021;29:100370.

Shang D, Sun D, Shi C, et al. Activation of epidermal growth factor receptor signaling mediates cellular senescence induced by certain pro-inflammatory cytokines. Aging Cell. 2020;19(5):e13145.

Simard FA, Richert I, Vandermoeten A, et al. Description of the immune microenvironment of chondrosarcoma and contribution to progression. Oncoimmunology. 2017;6(2):e1265716.

Su Z, Ho JWK, Yau RCH, et al. A single-cell atlas of conventional central chondrosarcoma reveals the role of endoplasmic reticulum stress in malignant transformation. Commun Biol. 2024;7(1):124.

Sun H, Zhang L, Wang Z, et al. Single-cell transcriptome analysis indicates fatty acid metabolism-mediated metastasis and immunosuppression in male breast cancer. Nat Commun. 2023;14(1):5590.

Takasugi M, Yoshida Y, Ohtani N. Cellular senescence and the tumour microenvironment. Mol Oncol. 2022;16(18):3333–51.

Tanaka M, Homme M, Teramura Y, et al. HEY1-NCOA2 expression modulates chondrogenic differentiation and induces mesenchymal chondrosarcoma in mice. JCI Insight. 2023;8(10):e160279.

Tiwari A, Trivedi R, Lin SY. Tumor microenvironment: barrier or opportunity towards effective cancer therapy. J Biomed Sci. 2022;29(1):83.

Tlemsani C, Larousserie F, De Percin S, et al. Biology and management of high-grade chondrosarcoma: an update on targets and treatment options. Int J Mol Sci. 2023;24(2):1361.

Wang L, Liu Y, Dai Y, et al. Single-cell RNA-seq analysis reveals BHLHE40-driven pro-tumour neutrophils with hyperactivated glycolysis in pancreatic tumour microenvironment. Gut. 2023;72(5):958–71.

Wang S, Ao L, Lin H, et al. Single-cell transcriptomic analysis of the senescent microenvironment in bone metastasis. Cell Prolif. 2024. https://doi.org/10.1111/cpr.13743.

Wu MH, Huang CY, Lin JA, et al. Endothelin-1 promotes vascular endothelial growth factor-dependent angiogenesis in human chondrosarcoma cells. Oncogene. 2014;33(13):1725–35.

Wu YY, Law YY, Huang YW, et al. Glutamine metabolism controls amphiregulin-facilitated chemoresistance to cisplatin in human chondrosarcoma. Int J Biol Sci. 2023a;19(16):5174–86.

Wu Z, Uhl B, Gires O, et al. A transcriptomic pan-cancer signature for survival prognostication and prediction of immunotherapy response based on endothelial senescence. J Biomed Sci. 2023b;30(1):21.

Xiong J, Dong L, Lv Q, et al. Targeting senescence-associated secretory phenotypes to remodel the tumour microenvironment and modulate tumour outcomes. Clin Transl Med. 2024;14(9):e1772.

Xu L, Saunders K, Huang SP, et al. A comprehensive single-cell breast tumor atlas defines epithelial and immune heterogeneity and interactions predicting anti-PD-1 therapy response. Cell Rep Med. 2024;5(5):101511.

Yang K, Guo W, Ren T, et al. Knockdown of HMGA2 regulates the level of autophagy via interactions between MSI2 and Beclin1 to inhibit NF1-associated malignant peripheral nerve sheath tumour growth. J Exp Clin Cancer Res. 2019;38(1):185.

Yin H, Jiang D, Li Y, et al. KDELR1 regulates chondrosarcoma drug resistance and malignant behavior through intergrin-Hippo-YAP1 axis. Cell Death Dis. 2024;15(12):928.

Yotsumoto F, Tokunaga E, Oki E, et al. Molecular hierarchy of heparin-binding EGF-like growth factor-regulated angiogenesis in triple-negative breast cancer. Mol Cancer Res. 2013;11(5):506–17.

Yu G, Wang LG, Han Y, et al. ClusterProfiler: an R package for comparing biological themes among gene clusters. OMICS. 2012;16(5):284–7.

Yuan C, Zhao S, Ma W, et al. SPP1 regulates SASP via the p53 signaling pathway to affect ALI progression. IUBMB Life. 2025;77(7):e70038.

Zając A, Król SK, Rutkowski P, et al. Biological heterogeneity of chondrosarcoma: from (Epi) genetics through stemness and deregulated signaling to immunophenotype. Cancers (Basel). 2021;13(6):1317.

Zhang S, Mo Q, Wang X. Oncological role of HMGA2 (review). Int J Oncol. 2019;55(4):775–88.